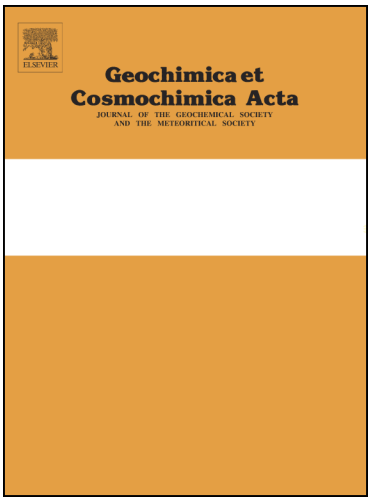

Reaction-induced porosity fingering: replacement dynamic and porosity evolution in the KBr-KCl system

Nicolas Beaudoin, Andrea Hamilton, Daniel Koehn, Zoe Kai Shipton, Ulrich Kelka

PII: S0016-7037(18)30242-4
DOI: https://doi.org/10.1016/j.gca.2018.04.026
Reference: GCA 10747

To appear in: *Geochimica et Cosmochimica Acta*

Received Date: 5 April 2017
Accepted Date: 26 April 2018

Please cite this article as: Beaudoin, N., Hamilton, A., Koehn, D., Kai Shipton, Z., Kelka, U., Reaction-induced porosity fingering: replacement dynamic and porosity evolution in the KBr-KCl system, *Geochimica et Cosmochimica Acta* (2018), doi: https://doi.org/10.1016/j.gca.2018.04.026

Reaction-induced porosity fingering: replacement dynamic and porosity evolution in the KBr-KCl system.

Nicolas Beaudoin[1,2*], Andrea Hamilton[2], Daniel Koehn[1], Zoe Kai Shipton[2], Ulrich Kelka[1]

1: School of Geographical and Earth Sciences, University of Glasgow, Gregory Building, Lilybank Gardens, G12 8QQ, Glasgow, UK;

2: Civil & Environmental Engineering, University of Strathclyde, 75 Montrose Street, G1 1XJ, Glasgow, UK

*Corresponding author: Nicolas.beaudoin@glasgow.ac.uk

Keywords: Mineralogical replacement; 3D-time Xray Computed Tomography; Porosity; reaction front; KBr; KCl; fluid-mediated replacement; Fingering.

Abstract

In this contribution, we use X-ray computed micro-tomography (X-CT) to observe and quantify dynamic pattern and porosity formation in a fluid-mediated replacement reaction. The evolution of connected porosity distribution helps to understand how fluid can migrate through a transforming rock, for example during dolomitization, a phenomenon extensively reported in sedimentary basins. Two types of experiment were carried out, in both cases a single crystal of KBr was immersed in a static bath of saturated aqueous KCl at room temperature and atmospheric pressure, and in both cases the replacement process was monitored in 3D using X-CT. In the first type of experiment a crystal of KBr was taken out, scanned, and returned to the solution in cycles (discontinuous replacement). In the second type of experiment, 3 samples of KBr were continuously reacted for 15, 55 mins and 5.5

hours respectively, with the latter being replaced completely (continuous replacement). X-CT of KBr-KCl replacement offers new insights into dynamic porosity development and transport mechanisms during replacement. As the reaction progresses the sample composition changes from KBr to KCl via a K(Br,Cl) solid solution series which generates porosity in the form of fingers that account for a final molar volume reduction of 37% when pure KCl is formed. These fingers form during an initial and transient advection regime followed by a diffusion dominated system, which is reflected by the reaction propagation, front morphology, and mass evolution. The porosity develops as fingers perpendicular to the sample walls, which allow a faster transport of reactant than in the rest of the crystal, before fingers coarsen and connect laterally. In the continuous experiment, finger coarsening has a dynamic behaviour consistent with fingering processes observed in nature. In the discontinuous experiment, which can be compared to rock weathering or to replacement driven by intermittent fluid contact, the pore structure changes from well-organized parallel fingers to a complex 3D connected network, shedding light on the alteration of reservoir properties during weathering.

1. Introduction

Reactions and phase transformations related to fluid-rock interaction are common in nature and important in diagenetic and metamorphic processes. Understanding the controlling mechanisms for phase transformations is key to accurately predicting the evolution of the physical parameters of rocks (porosity, permeability, and rheology) from centimetre-scale (e.g. porosity fingering in siltstones (Ortoleva, 1994)) to kilometer-scale (e.g. Dolostone geobodies (Merino and Canals, 2011)). Processes that are controlled by phase transformations vary from hydration of granulite (Centrella et al., 2015, 2016) to

weathering effects in building materials (Graham et al., 2015; Hamilton et al., 2008; Hamilton and Menzies, 2010) and industrial processes such as oil recovery using chemical reactants (Sheng, 2010), prediction of resource distribution (Dahlkamp, 2009), or CO_2 storage (Cailly et al., 2005). Replacement reactions have been extensively studied in the laboratory (Jonas et al., 2014; Kondratiuk et al., 2015; Merino and Canals, 2011; Ortoleva et al., 1987; Pedrosa et al., 2016a; Putnis and Putnis, 2007; Putnis and Mezger, 2004; Raufaste et al., 2010; Ruiz-Agudo et al., 2015), however this has mainly been done using high resolution techniques which require destructive sampling or are limited to 2D observation (e.g. Scanning Electron Microscopy in secondary-electron or backscattered-mode). Recent applications of X-ray computed micro-tomography (X-CT) in geosciences have developed temporally resolved 3D imaging (e.g. Cnudde and Boone, 2013). Here we apply X-CT to image the 3D structure of a replacement reaction and its evolution in an experimentally controlled environment. The focus of the X-CT imaging we used was on porosity development and reaction front propagation.

We use a highly soluble, cubic system: the KBr-KCl replacement (Kar et al., 2016; Putnis and Putnis, 2007; Putnis and Mezger, 2004; Raufaste et al., 2010; Spruzeniece et al., 2017). This system is well suited for temporal 3D imaging of replacement; it has a fast reaction time (hours) with visible porosity evolution and a stable end product. The KBr-KCl solid-solid replacement is an analogous system to assess the mechanism of dolomitization, where $CaCO_3$ is replaced by $Ca,Mg(CO_3)_2$ in a solvent mediated reaction, leading to the creation of porosity (e.g. in Kondratiuk et al., 2015). The KBr-KCl replacement exhibits an elongated anisotropic porosity that controls the replacement propagation (Kar et al., 2016; Raufaste et al., 2010). Fluid flow can extend pores to create the elongated structures (Kar et al., 2015; Raufaste et al., 2010), which are similar to finger pipes observed in nature during

dissolution (Szymczak and Ladd, 2009). Most experiments describe the phenomenon of the replacement but not the porosity evolution over time. Raufaste et al. (2010) showed for the first time that “cylinders” of elongated pores and reaction front-parallel discs develop and propagate into the replacing crystal by local dissolution-precipitation reactions. In this contribution we quantify the larger-scale three-dimensional porosity evolution over time and study the effects of continuous versus discontinuous replacement. Pattern evolution during replacement reactions induced by infiltration of fluids can be complex, with initial roughening leading to localisation or fingering of reacted parts which forms fingers in 3 dimensions. Fingers are the results of a positive feedback loop between dissolution or shrinking of material and an increase in porosity and thus faster or more localized infiltration of fluid accelerates the reaction and propagation of fingers. The creation, amplification and abandonment of fingers depends on the ratio between advection and diffusion (Péclet number), the ratio between advection and reaction speed (Damköhler number) and internal surface area from the generation of porosity (Szymczak and Ladd, 2013). These parameters also impact the reaction front thickness and roughness in replacement systems (Ortoleva et al., 1987). Dolomitization and dynamic structure evolution during replacement is of particular interest to the hydrocarbon and mining industry, as dolostone geobodies are among the most studied non-conventional reservoirs and host ore bodies (Merino and Canals, 2011; Montaron, 2008; Whitaker et al., 2004).

In this work, we examine the KBr-KCl fluid mediated replacement reaction in detail, we quantify the porosity evolution through time, and compare experimental data with numerical predictions using mass balance solubility calculations. The high-resolution 3D dataset of the temporal evolution of KBr-KCl replacement reaction with X-CT allows key observations in order to refine our understanding about how much porosity develops during

the replacement, how porosity is distributed over time, and how the reaction front progresses into the crystal. These quantitative observations complement previous works (Kar et al., 2016; Raufaste et al., 2010) and allow us to better understand the dynamics of the replacement propagation and associated mechanisms, such as volume change, porosity geometry and transport regime. By comparing two sets of experiments that mimic two different environments for fluid-rock interactions (single event versus intermittent flow), the phenomenon we describe and quantify can ultimately be transferred to other natural systems.

2. Experimental design

1. Replacement experiment

A polished single crystal of pure KBr (optical quality, from Korth Kristalle GmbH, Germany) was cut into rectangular cubes with dimensions of ca. 3.5 mm x 3 mm x 5 mm (Fig. 1-a). A saturated solution of KCl (333 g/kg of water) was made from reagent grade KCl (MERCK 99.5%) and Mili-Q water (18.2 MΩ). The solution was filtered through a 0.45 µm membrane and kept at a constant temperature of 20°C. Two sets of experiments were designed to investigate: the reaction in stages (set 1), and a complete reaction without interruption (set 2). In set 1 a weighed prism of KBr was completely immersed in aqueous KCl, covered with a watch glass and left to react for 55 minutes under ambient conditions. During the 55 minutes, the sample was removed from the bath for X-CT scans at t=5, 10, 20, 35, and 55 minutes of cumulative reaction time. Upon removal from the bath, the sample was immediately placed on absorbent paper under a gentle stream of air, in order to halt the reaction and limit precipitation by evaporation inside the sample to a level that is below

the detection resolution of the X-CT. The prism was then weighed before being placed in the X-CT, where it was scanned for 2 hours, then weighed again and returned to the covered bath. The experiment was repeated with a new crystal using the same experimental and environmental conditions to test reproducibility. Set 2 experiments were designed to determine how reaction interruption, necessary for X-CT scanning, induced alteration in the replacement process. To do so 3 weighed samples were allowed to react for a set duration (15 minutes, 55 minutes, and 5.5 hours) without interruption. Then they were removed from the bath, placed on absorbent paper under a gentle stream of air to halt the reaction, weighed, and scanned under the same conditions as experiment set 1. A second batch of continuous replacement experiments was conducted for 2 samples which were immersed for 15 and 55 minutes to ensure repeatability of the observed phenomenon. The mineralogy of the reaction zone was determined by XRD (Bruker, D8 Advance) using samples from the continuous experiment after t=55 minutes of reaction time and after complete replacement (t=330 minutes). To assess features which may be below the resolution of X-CT, a sample of the set 1 experiments (t=15 minutes) was cut in half after the scan, and investigated under optical microscopy.

2. 3D X-CT imaging

The X-CT scans were performed using a Nikon XTH 320/225 system, equipped with a 225 kV reflection gun, a micro-focus Ag target, and a 2000*2000 pixel flat panel photodetector (cell size 0.2 x 0.2 mm). The sample was placed on the rotation stage in the same position as it was in the bath during replacement, meaning the bottom of the scan represents the surface of contact between the sample and the glass beaker during the replacement. The X-ray source-to-sample distance was set to achieve the minimum voxel size of 3 μm. Scanning

conditions were an accelerating voltage of 140 keV, 20 μA current (power 2.8 W) using a Ag target with no metallic filter. The exposure time for each projection was 1.41 seconds, lasting for 3141 projections with a scan-time of 2 hours (1 frame per projection).

3. Volume reconstruction, correlation and image segmentation

3D volumes were reconstructed from projections using the CT Pro 3D software (© 2004-2016 Nikon Metrology), with an automatic reconstruction tool to find the scan's centre of rotation, and applying a beam hardening correction (Brooks and Dichiro, 1976). Ring artefacts, which are common in micro X-CT, are barely present and did not affect the segmentation process. Each reconstruction is 1200*1200*1700 pixels and all volumes were reconstructed in 16 bits (65536 grey values). 3D volumes were further analysed using Avizo (v.9.2.0, © FEI). First, the noise was reduced by appliying an edge-preserving smoothing filter ("bilateral filter") that averages the intensity value of a voxel with regard to the intensity value of its neighbours, considering a number of neighbours defined by a 3x3x3 kernel size (3D interpretation). Second, the 5 volumes from the scans of the discontinuous experiments were manually aligned in the same project, using translation, rotation, then the software-assisted registration tool (Fig. 2a). Alignment of the volume is based on the superposition of the straight limits of the sample on its 6 sides, and on some immobile limit of pores (Fig. 2b). This step is vital in order to ensure a meaningful comparison of the features, from which our interpretation of the internal structure evolution through time is derived.

Image segmentation of mineral phases in the X-CT volume is based on the atomic number and the density of the phase, which is represented in grey scale, with brighter shades indicating higher density and atomic number. The threshold tool was used to label the scan onto the reacted volume (dark grey on the scan; red, light blue and blue on Figs. 2c,

3), the non-reacted volume (light grey on the scan, green on Figs. 2c, 3), and surrounding air (black, not represented on Figs. 2c, 3). From this segmentation, the reacted part of the volume was split into two: a less dense phase inside the sample (blue) and a denser phase toward the exterior of the sample (red). In order to segment the porosity (dark grey/black, light blue in Figs. 2c, 3) in each of the two reacted parts, pixels were selected depending on a threshold, and then selected pixels attributed to noise were removed. The removal was performed using the ''remove small spot'' function, which consists of deleting all clusters of less than 10 pixels from the segmented 3D data. The segmentation method is efficient, even if some visible pores in the innermost part of the reacted zone of the sample could not be segmented, because they were below the limit of resolution, producing to a grey value representing a mix between the pore and the solid crystal (Fig. 3). This below-the-resolution problem is an X-CT limitation, which was counterbalanced by considering our porosity measurements as the minimum volume. Higher resolution observations in 2D from literature sources were taken into account, in addition to our own microscopic observations of the reaction front porosity (Fig. 3c ;Kar et al., 2016; Putnis and Putnis, 2007; Putnis and Mezger, 2004; Raufaste et al., 2010). Once the labelled zone was defined, a voxel count was used to define the volume occupied by each voxel category (red, light blue, blue and green), which allowed quantification of each phase in the sample.

To ensure a reliable quantification of segmented phases, three regions of interest were defined in the reconstructed volumes: 1) the whole scanned volume (2000*2000*2000 voxels), minus 900 microns at the bottom, 2) 2mm side length cubes and 3) 500 micron side length cubes. All regions of interest include the domains shown in figure 3. Additional datasets were reconstructed using slightly different threshold values to test the accuracy of the segmentation. The result was that the combined effect of threshold variation and of the

noise removal routine was found to be negligible (< 5% of the reconstructed volume for each phase). This test was done for both batches of experimental sets, and we used average values to represent the volume of each phase, with the standard deviation reported in figure 5 as error-bars (Table 1, Fig. 5). To assess the connectivity of pores, all the voxel gatherings belonging to the porosity category were labelled with a unique colour as an individual feature, highlighting the connected pore volumes. The statistical distribution of the pores is shown as whisker box plots (Fig. 5). Morphological measurements of the pores were conducted from the 3D dataset (e.g. Anovitz and Cole, 2015). The length and the width at half the length were measured on 2D sections of isolated pores (e.g. Fig. 3), in two orthogonal dimensions. Results were used to define an aspect ratio α=length/width, averaged for each replacement step (Table 1).

3. Results

The KBr reaction with KCl resulted in pseudomorphic replacement of KBr with K(Br,Cl) and finally KCl (Figs. 2, 3). The optical quality single crystal of KBr loses transparency from the light scattering effect of small crystallites of K(Br,Cl) and becomes bright blue (Fig. 1), due to an anion vacancy in the sample lattice being filled by unpaired electrons. This phenomenon is known as a colour centre, or F-centre, and is extensively described in NaCl and in KCl samples (Putnis, 1992). This phenomenon does not affect the X-CT scan quality, even though the existence of such defects in the sample lattice is likely to control diffusion (Putnis, 1992). The activation of a colour centre occurred in all our experiments, implying the comparison between sets remain valid. Both continuous and discontinuous experiments are duplicated, and duplicates show the same replacement and porosity evolution, with similar results from segmentation and quantification, showing that any possible artefacts from

drying have not affected the scan results. All values derived from the X-CT voxel counts are reported in table 1.

Once the reaction starts, the reacting crystal can be segmented into 4 domains of different atomic density and porosity (Fig. 4), starting from the inside towards the outer rim:

- The unreacted crystal of KBr (domain 1), which has the highest density.
- The reaction zone, where visible porosity (Fig. 2, 3, 4) develops due to the disparity between the molar volume of KBr (43.3 g/cm^3) and KCl (27.1 g/cm^3). This zone can be split into two domains (domains 2 and 3). Domain 2 starts with a rough/smooth boundary between the reacted volume and the unreacted volume (the reaction front), and is characterized by the second highest density (more Br than Cl) and apparently disconnected, pseudo-circular visible pores. In addition this domain contains a high density of cubic primary fluid inclusion (Fig. 4c), small below-the-resolution pores, and flat, disc-shaped pores (Fig. 3b), oriented normal to the elongated pores we refer to as fingers. The elongated fingers are characteristic of domain 3, where the solid phase has a lower density as it incorporates more Cl.
- A precipitate layer of the same density as domain 3 but with a porosity below the limit of our resolution (i.e. pores smaller than 216 μm^3). This domain 4 consists of material that precipitated during the drying phase when the sample was taken out of the bath to be scanned and consequently increases it's thickness after each bath (Fig. 2b).

3.1. Results for set 1 – discontinuous experiment

During the successive steps of the replacement, the observed mass loss, reaction propagation and porosity development are non-linear (Fig. 5). 50% to 70% of crystal alteration occurs within the first 10 minutes of the reaction which results in 23% mass loss, a development of 20% local porosity, and 30% of the original crystal volume is replaced. At t=55 minutes of the reaction, the total mass loss reaches 33%, the local porosity reaches 30%, and the reaction zone affects 50% of the initial crystal volume. Domain 2, that separates the porous reacted domain from the unreacted KBr (Figs. 3, 4), steeply increases in average thickness during the first 20 minutes of the reaction (from 0 to 53 microns) and then increases more gently (up to 75 microns at t=55 min, Fig. 4d, table 1). The front shows a rough interface (t=5 and t=10 min) that becomes smooth before t=20 minutes of reaction (Figs. 2, 4). The evolution of the volume replaced (v) during the reaction at a time t>5 min follows a $v=t^{0.5}$ function, which suggests that the replacement is a diffusion-limited process (Fig. 5b).

The porosity evolution is quantified at each step of the solid reaction (Figs. 5a, 7, Table 1) for the sample (i.e. the whole volume) and for the reaction zone (i.e. focusing on domains 2 and 3). While the porosity in the reaction zone reaches its maximum value (ca. 30%) at t=35 minutes, the overall porosity increases at a slow rate, from 10% at t=10 to 22% at t=55 minutes. This evolution is a result of the propagation of the porous reaction zone into the crystal during the whole experiment. In the first 10 minutes the porosity appears to develop perpendicular to the sample surface (Fig. 2b, c) forming fingers that propagate inwards, before gradually evolving to surface-parallel elongated pores that increase the 3D connectivity. It is worth noting that fewer fingers develop in the crystal corners where interaction between fingers perpendicular to each other is visible (Figs. 2a). The evolution of pore connectivity in the sample is estimated by the size of the biggest connected pore that

was obtained through the segmentation process. The statistical distribution (Fig. 6) shows that despite having a decreasing median value the total volume of the largest pores increases during the reaction, leading to an overall increase in pore connectivity. At t=20 minutes the median volume of pores has decreased while the size of the largest pores had increased, suggesting the development of numerous small disconnected pores in the crystal, consistent with the observable thickening of the reaction front (Fig. 5). In addition, we observed that the outside edge of the pores progressively migrated towards the inside of the volume leaving an outer rim of precipitated K(Br,Cl) within which the porosity is below our detection limit (216 μm^3, Figs. 2c, 3, 4). This rim (domain 4) gets thicker in the first three baths before stabilizing at ca. 70 microns, suggesting it does not significantly dissolve once the sample is put back in a new bath. The evolution of finger spacing is reported in Figure 8, the radius of fingers increases as the density of fingers decreases with time, suggesting they get wider and connect laterally. The average aspect ratio evolution of the fingers show a rapid decrease after 10 minutes, with values of α getting closer to 1 (i.e. spherical), supporting the lateral connectivity of the fingers.

3.2. Results for set 2 – continuous experiments

In the set 2 experiments, samples have been reacting continuously before being scanned, resulting in snapshots of the replacement for three different crystals at three different times (15, 55 and 330 minutes, Figs 9, 10, table 1). Mass loss increases slightly, from 24.5% at t=15 minutes, 26% at t=55 minutes to 50% at t=330 minutes (upon complete replacement). The volume of the reaction zone increases too, from ca. 30% at t=15 min to ca. 55% at t= 55 min. The porosity increases with time: 24.5% at t=15 min to 34.5% at t= 55

min in the reaction zone only, and 12% at t= 15 min to 29% at t=55 min if the whole crystal is considered. Once the reaction is complete, we observe pores which elongate from the outer walls towards the middle of the sample, representing 55% of the initial volume, divided into empty pores (29% of the total volume) and a coating made of reaction products (26% of the total volume, Fig. 9). The reaction front is rough at both times (15, 55 min) and domain 2 is thin (70 microns). The outer deposit formed during the drying process is still present, but in all cases we observe the same final thickness regardless of the duration of the reaction (70 microns).

In these set 2 experiments we observe that the porosity developed as elongated fingers perpendicular to the sample walls (Figs. 9, 10). The average aspect ratio is similar at t=15 and 55 minutes of reaction, showing elongated fingers, 10 times longer than their width. At the corners of the crystal, the competition between fingers from the two orthogonal surfaces of the crystal results in the inhibition of finger development (Fig. 9a). Once the reaction is complete, the interaction between fingers growing from opposite sides can be seen (Fig. 10) and fingers coarsen. The average aspect ratio decreases to a value of 6, due to the coarsening of the fingers that cannot elongate further into the crystal. There is less outer deposit related to the drying process in this experimental set than in the last stage of set 1 experiments, and the shape of the whole sample was perfectly conserved.

XRD measurements shows that the reaction zone consists of K(Br,Cl) with 50% of Cl substituting Br in the mineral lattice after 55 minutes and the nearly completely replaced sample is 90 wt % KCl after 330 mins.

3.3. Results of analytical modelling

Using solubility and density data (Durham et al., 1953, Dejewska et al., 1998), we calculate porosity increase and the mass fraction of KCl substitution in the solid KBr crystal. The system is adiabatic and accounts for mass conservation of the complete system (i.e. solution and crystal). The initial condition is defined by mass, volume and density of the original KBr crystal (0.144 g, 0.053 cm^3 and 2.75 g/cm^3). The calculation is iterated over 100 time steps for volumes of saturated KCl solution of 0.01 – 1000 ml to derive a relationship between porosity evolution and solid KCl replacement (Fig. 11). The relationship is non-linear (solid line in figure 11), because the solubility of the KCl-KBr solution varies with composition, as does the crystal density. The calculation is in line with the experiment as XRD shows 50% Br-Cl substitution after 55 minutes of reaction and the reconstructed porosity is ca. 35% of the reaction zone at that time step (Set 2, Table 1). Our calculation (Fig. 11) predicts that the porosity created at 50% Br-Cl substitution in the reaction zone is 37%. This allows us to apply the model to predict the Br-Cl substitution in the reaction zone at a measured porosity value (crosses and circles on figure 11, values are from Table 1). The output of the model clearly shows the relationship between the mass fraction of replaced KCl and the subsequent porosity development. The mass fraction of KCl is calculated according to *mfKCl = mKCl/(mKCl+mKBr)*, where *m* is grams of the corresponding phase. Upon complete replacement of KBr by KCl, the calculted porosity is 46%, in line with what is inferred by the continuous replacement experiment where 55% of the volume is pore space (29%) plus product coating from drying (26%). The analytical calculation does not take into account crystallisation from evaporation of the solution phase.

4. Discussion

4.1. Reaction front migration

The replacement of KBr by K(Br, Cl) in the presence of KCl-H_2O solution is an interface-coupled dissolution-precipitation process as defined in Putnis and Putnis (2007). In this type of process the concentration gradient in the solution triggers replacement and the bulk volume is conserved because the dissolution is coupled to precipitation with the chemical reaction occurring at the interface layer between fluid and solid (Putnis, 2009). It is out of the scope of this paper to discuss the mechanisms that allow the volume preservation during the replacement, as this is extensively discussed elsewhere (Putnis and Putnis, 2007; Raufaste et al., 2010; Pollok et al., 2011; Merino and Canals, 2013; Kondradiuk et al., 2016; Spruzeniece et al., 2017). We observe a replacement zone next to the reacted/unreacted front which exhibits a high density of cubic fluid inclusions. This occurrence marks an intense precipitation process and supports our conclusion that the dissolution/precipitation occurs in a limited zone of the sample (domain 2 in our results).

Our time-lapse 3D monitoring of successive reaction propagation in single samples shows two distinct phases. The first 10 minutes (first phase) are characterized by a) a rapid mass loss, porosity increase and propagation of the replacement front plus b) a rough contact between reaction front and unreacted sample, c) by a rapid increase of the reaction front's thickness (from 0 to 53 microns, Fig. 2, Table 1), and d) a stable morphological aspect ratio. After 10 minutes (second phase), the mass loss and replacement propagation in the volume are much slower (Fig. 5), and show a decreasing aspect ratio. In this second phase the contact between reacted and unreacted zones is smoother and the thickness of the reaction front increases slowly (Fig. 2). An initial phase with fast replacement of about 10 minutes followed by a second phase with slower replacement has also been reported in previous KBr, KCl replacement experiments (Kar et al., 2016).

The initial infiltration of fluid into the crystal is fast and probably driven by the volume change and subsequent porosity increases during the reaction. This produces a fast propagation of the front and a rough front with elongated fingers, which is the product of a positive feedback loop between the fast supply of reactant and the porosity created. The second regime shows a smoothening of the front, slower propagation and the thickness of the reacting zone stabilizes. These observations are typical for a diffusion dominated process where solute transport is too slow to produce new fingers, which will then coarsen, and the thickness of the reacting zone is defined by the scale of the effective diffusion. The rate of change of the reaction front thickness and its overall roughness decrease, coupled with the decrease in rate of replacement and mass loss, are indicators for a transition in the transport regime, from local advection-driven to diffusion-limited (Lichtner et al., 1996; Ortoleva, 1994; Ortoleva et al., 1987; Steefel et al., 2005; Steefel et al., 2015; Szymczak and Ladd, 2013). Relationships between pore aspect ratio of the fingers and the Péclet number were established (Dutta et al., 2006) and the observed decrease in the aspect ratio in our set 1 experiment indicates that the ratio between advective transport rate and diffusive transport rate decreases with time. Such a transition is not observed in experiment set 2 before the complete replacement, which is supported by a constant aspect ratio, because KBr crystals go through one reactant bath only, so the precipitate layer that forms during drying is never re-immersed in solution. Thus, the transition from advection- to diffusion-driven transport is likely to be related to the thickening of the precipitate outer layer produced during the drying time required for scanning (Figs. 2, 4, 5) in experiment set 1. Kar et al. (2016) have shown that transport of matter in the fingers can be relatively fast because convection cells develop in the fingers due to electro-kinetics (as explained in detail in section 4.2.2). We propose that this precipitate layer, characterized by the absence of pores bigger than 216

μm^3, disturbs and slows these convection cells. This limits the supply of reactants in the fingers, and as the finger-scale advection efficiency diminishes with distance from the KCl source, fingers stop growing perpendicularly to the crystal wall. At this point elementary diffusion governs the reaction propagation, leading to slower replacement propagation, a porosity morphology getting wider, a smooth front and thicker reacted zone (Figs. 2, 4, 5, 13).

4.2 Finger development

4.2.1. Initial porosity localization

Because of the volume difference between both atoms, Br-Cl substitution leads to a volume loss forming porosity. Figure 11 reports the calculated porosity creation during the substitution evolution. 3D scans in both sets of experiments show that the mm-scale porosity develops as fingers (Figs. 2, 9, 11). Fingers form due to the positive feedback of dissolution-driven flow, when initially spherical pores (as observed in the front, Fig. 3) connect and form pipes acting as channels. The fluid flow is faster in the pipes than in the initial KBr crystal, and as a result the fluid-mediated replacement reaction is more efficient at the tips of the pipes, where chemical gradients are larger (Figs. 12, 13). This mechanism of finger formation is described in numerous systems related to dissolution processes such as NaCl-H_2O (Ortoleva et al., 1987; Renard et al., 1998), or in karst, caves or fracture dissolution (Kondratiuk et al., 2015; Petrus and Szymczak, 2016; Raufaste et al., 2010; Szymczak and Ladd, 2006, 2009; Szymczak and Ladd, 2013).

4.2.2 Self-generated fluid flow

The fingers we observe differ from reactive-infiltration wormholes (i.e. dissolution) in the sense that they go through less competition during growth, *i.e.* they don't seem to grow at the expense of others, as dissolution wormholes would (Szymczak and Ladd, 2006; 2009).

Competition behaviour is typical of reactive infiltration and is related to the pressure gradient created by an externally imposed flow (Szymczak and Ladd, 2009). Although our experimental setup does not have assisted fluid flow, we observe channels, which implies a crystal-scale flow (Putnis and Putnis, 2007; Putnis, 2009; Pollok et al., 2011; Kondratiuk et al., 2015), meaning that the system generates a fluid flow at the mm-scale and below. Self-triggered fluid flow has been described for the replacement of KBr by KCl and is interpreted as electro-kinetic fluid flow (Kar et al., 2016). This phenomenon is explained by the diffusion-osmosis mechanism, where convective cells are generated by an ionic gradient, in this case between K^+, Br^-, and Cl^- which creates an electric field because the ions have different diffusion coefficients (Ajdari and Bocquet, 2006, Kar et al., 2015, Kar et al., 2016, Plumper et al., 2017). Such a convective cell is required in the case of the KBr - KCl pseudomorphic replacement because it allows Cl^- to go in and Br^- to come out, so that porosity can develop. The fingers enhance the thickness of the reaction zone significantly by dynamically affecting the chemical gradient (Fig. 12b). Without fingers the reaction zone would be limited by the diffusion length scale and the crystals would not be replaced completely (Fig. 12a). The addition of fingers allows the reaction zone to migrate into the crystal and replace the whole crystal in relatively short time scales.

4.2.3 Porosity evolution and coarsening

Real time observation using microscopy, as presented in Raufaste et al. (2010) shows similar finger-like geometries to the ones we observe (Fig. 3c, Fig. 6 in Raufaste et al., 2010), except for the connected trail of pores at the finger tips and they also observed the occurrence of disc-shaped pores which are oriented perpendicular to the fingers. Raufaste et al. (2006) interpret these discs as shaping the porosity cylinders observed to develop during the phase-transformation process. Because of the limited resolution of the X-CT, we cannot

see those cavities (discussed below), yet we can see, but cannot segment, the small pores that link the tip of the finger to the replacement front (e.g. Figs, 3c; 9b). Optical microscopy, as presented in figure 3c, shows a higher magnification of the reaction front and illustrates that some of the pores in our experiments are similar to those found by Raufaste et al. (2010) with small, potentially disc- like pores that are oriented perpendicular to the fingers (Fig. 3b, 4c). The actual reaction front seems to be more rough and less organized than the one reported by Raufaste et al. (2010) indicating that the replacement process may not be as organized as presented in the Raufaste model (Fig. 3b). The use of 3D imagery allows us to study the evolution of the spacing and size of the fingers and illustrates coarsening occurs during the experiments (Fig. 8). Coarsening of similar structures has been observed in a number of systems, for example in other fingering processes (Kondratiuk et al., 2017; Menon and Otto, 2005), and also in anti-cracks driven by stress shielding (Koehn et al., 2003) and surface wave coarsening in stressed crystals (Koehn et al., 2004), and carbonate acidizing (Gohmmem et al., 2015). The fingering mechanism active in KBr-Cl replacement is then behaving like a normal fingering process, thus it is possible that such a mechanism affects other natural systems. We interpret coarsening of the fingers as a phenomenon linked to the elongation of the fingers. When the fingers are too long for the reactant to be efficiently delivered to the tip, then the chemical gradient at the wall of the finger overcomes the chemical gradient at the tip (Fig. 12). The latter effect results in a more efficient replacement and porosity development at the finger walls, which produces coarsening. The decrease in the Péclet number that accompanies the coarsening, highlighted by the aspect ratio evolution, supports that the latter is related to the decrease in the advective transport rate. The experiment sets presented here show different pore and finger coarsening. In experiment set 1, coarsening is related to the development of the precipitate layer that

reduces the influx of reactant and results in a lateral elongation of the pores parallel to the wall of the crystal (Figs. 2, 7, 13). In experiment set 2, where a precipitate layer does not disturb the reaction, we observe that the fingers need to reach a certain length (normal to the crystal's walls) before neighbouring fingers fuse together and eventually connect when they have reached their maximum size (Figs. 9, 10, 13). Finger coarsening over time in experiment set 2 is characterized by a power law with a coarsening factor of 0.4 to 0.5 (Fig. 8f), which fits within the range observed for fingering in natural systems (Menon and Otto, 2005; Kondratiuk et al., 2017). Thus, the KBr-KCl related porosity creation as finger behaves as a classical fingering process.

By inducing an overgrowth on the edges of the crystal during replacement, similar to rock weathering, we can discuss the impact of finger development in a diffusion-limited system. The differences in the dynamic of the replacement and of the pore morphology, with or without this overgrowth, highlight that the pore-scale advection cells allow for a faster and larger replacement at the crystal scale (Figs. 12, 13).

4.3 Comparison with other natural systems

4.3.1 Experimental studies

Our experiment sets show that the reaction propagation is diffusion-limited, in line with previous work on the same system (Putnis and Putnis, 2007; Raufaste et al., 2010), where fingering is observed (Putnis and Mezger, 2004; Raufaste et al., 2010; Spruzeniece et al., 2017), and with work on a single crystal of calcite replaced by calcium sulphate (Ruiz-Agudo et al., 2015). Also, the porosity fingering process is observed in polycrystalline systems, such as marble replaced by phosphates (Pedrosa et al., 2016a; Pedrosa et al., 2016b).

4.3.2 *Discontinuous replacement: porosity alteration.*

The overgrowth in our experiment leads to a striking change in the anisotropy of the connected porosity once the pore-scale advection cells are not efficient anymore (after ca. 10 minutes). Such replacement-related porosity anisotropy is likely to happen when replacement was partial or originated from intermittent contact with the reactant, e.g. in Sachau et al. (2015). This has a theoretical impact on later fracture development in rocks, as changes in mineral phases alter the mechanical properties of rocks (Barbier et al., 2012; Laubach et al., 2009). Distribution and anisotropy of porosity affect the accommodation and propagation of deformation (Robion et al., 2012) as well as the fluid distribution in a solid (Koehn et al., 2006). In our case, stress applied to the sample before the replacement or after could potentially result in different fracture orientation, related to porosity evolution and may lead to stress-enhanced finger development (Koehn et al., 2004). Recent findings show that the distribution of porosity can create microstructures in crystal lattices as a consequence of replacement (Spruzeniece et al., 2017), which has the potential to mislead geologists when using microstructures to reconstruct deformation history.

Set 1 experiments can also be compared to rock weathering (Putnis, 2015). Weathering is especially important in buildings and sculptures because it can erode fine detail, change the appearance of the building or cause significant surface granulation (Hamilton et al. 2008, Hamilton et al. 2010). Set 1 experiments show that the development of such an outer layer is related to enhancement of the lateral connectivity and prevents wall-perpendicular fingers developing further (Fig. 13). This is directly related to pore clogging in the outer rim of the sample (Fig.1, 3). Pore clogging has been observed in

calcareous sedimentary building stones exposed to sulphurous gases, which allows gypsum ($CaSO_4.2H_2O$) to precipitate in and block the pores (Fookes et al., 1988). This porosity shape control also has an impact when it comes to assessing the structural integrity or reservoir properties of rocks which have been replaced and exposed, as the internal porosity of a shallow rock (i.e. cm below the weathering zone) can be different to that of deeper buried samples. Beyond civil engineering, our set 1 experiment can be compared with weathering of natural rocks, such as salt weathering in porous stones (e.g. Benavente et al., 2001), which will affect the reservoir properties of rocks (Goudie, 1999) and impact on geomorphological processes (Goudie and Viles, 1997).

4.3.3 Continuous replacement: enhanced replacement

Continuous replacement in the KBr-KCl system leads to the creation of 29% unclogged porosity and to the complete substitution of Br by Cl. The formation of pore space in this system is similar to dolomitization, where the created porosity ranges from 13% to 25% (Merino and Canals, 2011; Kondratiuk et al., 2016). Dolomitization is an important process in sedimentary basins, reservoir rocks (Al-Helal et al., 2012; Ferket et al., 2003; Gomez-Rivas et al., 2014; Machel and Buschkuehle, 2008; Machel and Mountjoy, 1986; Maliva et al., 2011; Montaron, 2008; Whitaker et al., 2004) and ore bodies (Bons et al., 2014; Kelka et al., 2015; Kelka et al., 2017; Merino, 2006; Merino and Canals, 2011; Nielsen et al., 1998). Questions about the mechanisms that govern dolomitization of large geobodies are debated, and focus on how the huge amount of magnesium required to complete the replacement could enter the system, without involving billions of cubic meters of fluid. A solution to this problem is the existence of large scale convective cells of magnesium rich fluids, which can deliver enough reactant to replace the volumes we observe today (e.g. Gomez-Rivas et al., 2014).

Our experiments illustrate how crystal-scale, self-triggered convective cells can develop and enhance the replacement in natural systems. The development of fingers significantly increases the reaction zone and allows the complete crystal to be replaced. We propose to term this process reaction-induced porosity fingering, adding the term fingering to the accepted "reaction-induced porosity" terminology to reflect the geometry of the pores, and suggest that it is a process similar to fracture enhanced replacement where fluids can infiltrate through fractures instead of fingers. The main difference between fracturing and fingers is the geometry, fingers are ideal for fluid transport into the system whereas fracture networks would potentially form tessellation and lead to basalt column-like geometries, which are more complicated. Our observations open the way for a novel theory of dolomitization processes and further investigations are now required to validate that small-scale self-triggered convective cells can lead to the replacement of massive geobodies observed in nature. Similar mechanisms of reaction-induced pores and electro-kinetic transport have been revealed to be efficient in feldspar, that leads to pervasive and efficient pathways for fluid flow in tight rocks (Plumper et al., 2017). Thus, the reaction-induced porosity fingering mechanism could potentially explain how large volumes can be replaced with limited fluid supply in low permeability systems, like dolomitization, or eclogitization of tight granulite, for example.

5. Conclusion

We performed 2 sets of replacement reaction experiments, a discontinuous and a continuous one, and monitored the dynamics of the systems using successive X-CT 3D reconstructions of pseudomorphic KBr- KCl replacement. Time-lapse monitoring of the reaction allowed us to develop a novel understanding of dynamic porosity distribution and

replacement mechanisms which we term reaction-induced porosity fingering from the following observations:

- 5 different phases in the experimental samples can be distinguished based on atomic number and density: (1) KBr sample, with no pores or visible defects; (2) K(Br,Cl) (more than 50% Cl substitution) phase, with connected elongated pores; (3) K(Br,Cl) (less than 50% Cl substitution), with disconnected, pseudo circular pores; and (4) Porosity. (5) pure KCl resulting from complete replacement. An external deposit related to sample drying is also observed.
- For the first time, we are able to quantify the porosity created during the replacement. While the crystal porosity increases during the replacement progression in the sample (up to 55% porosity after complete replacement of the crystal), the actual porosity in the replaced part is stable after around 35 minutes into the experiment, with a value of 30% (+/- 5%).
- Porosity develops as elongated fingers normal to the crystal walls implying that a self-generated convective fluid flow exists in the fingers. This diffusion-osmosis mechanism allows the reactant to go in and the replaced material to be washed out, and leads to local, pore-scale, advection dominated dissolution-precipitation.
- When the crystal develops a thick outer precipitate induced by drying and reflecting weathering or pulse of reactant (set 1), we observe at first a rapid replacement phase (first 10 minutes) affected by local advection and characterized by a rough, thin reaction front, and a second slow replacement phase likely governed by diffusion, characterized by a smooth, thick reaction front.
- Fingers eventually connect laterally when (1) fingers cannot elongate any further (continuous experiments), or (2) when a precipitate gradually forms at the outer rim

of the crystal (discontinuous experiments). In the latter, the lateral connectivity changes the polarity of the highest permeability and therefore the theoretical direction of potential posterior fluid flow. This observation must be taken into account when dealing with weathered rock, particularly for characterization of replaced reservoir rocks.

Our experimental approach to the KBr-Cl replacement show that both the difference in replacement rate and pore development in our two sets of experiments can be explained by the formation of a localized porosity with a shape similar to dissolution fingers. This is an important mechanism that could control the speed and spatial extension of diffusion-limited processes such as replacement in natural rock systems and weathering. From this point of view, that mechanism can be used to reassess our understanding of key problems in geosciences, e.g. hydrothermal dolomitization or hydration of tight rocks.

Acknowledgment

Authors thank the five anonymous reviewers and the associate editor Pr. Anovitz for their comments that strongly improved the quality of this manuscript. Authors thank the Scottish Funding Council's Oil and Gas Innovation Centre for funding the X-ray Computed Tomography scanner. NB is funded by the Oil and Gas Innovation Centre and the University of Strathclyde. This project has received funding from the FlowTrans ITN, European Union's Seventh Framework Programme for research, technological development, and demonstration under grant agreement 316889. All data used in this paper are available upon demand to the corresponding author (Nicolas.beaudoin@glasgow.ac.uk).

References

Al-Helal, A.B., Whitaker, F.F. and Xiao, Y. (2012) Reactive transport modeling of brine reflux: dolomitization, anhydrite precipitation, and porosity evolution. Journal of Sedimentary Research 82, 196-215.

Anovitz, L.M., and Cole, D.R. (2015) Characterization and Analysis of Porosity and Pore Structures. Reviews in Mineralogy and Geochemistry 80, 61-164

Benavente, D., del Cura, M. G., Bernabéu, A., and Ordóñez, S. (2001) Quantification of salt weathering in porous stones using an experimental continuous partial immersion method. Engineering Geology 59(3-4), 313-325.

Bons, P.D., Fusswinkel, T., Gomez-Rivas, E., Markl, G., Wagner, T. and Walter, B. (2014) Fluid mixing from below in unconformity-related hydrothermal ore deposits. Geology 42, 1035-1038.

Cailly, B., Le Thiez, P., Egermann, P., Audibert, A., Vidal-Gilbert, S. and Longaygue, X. (2005) Geological storage of CO2: A state-of-the-art of injection processes and technologies. Oil & gas science and technology 60, 517-525.

Centrella, S., Austrheim, H. and Putnis, A. (2015) Coupled mass transfer through a fluid phase and volume preservation during the hydration of granulite: An example from the Bergen Arcs, Norway. Lithos 236-237, 245-255.

Centrella, S., Austrheim, H. and Putnis, A. (2016) Mass transfer and trace element redistribution during hydration of granulites in the Bergen Arcs, Norway. Lithos 262, 1-10.

Cnudde, V. and Boone, M.N. (2013) High-resolution X-ray computed tomography in geosciences: A review of the current technology and applications. Earth-Science Reviews 123, 1-17.

Dahlkamp, F.J. (2009) Uranium Deposits of the World. Springer, Berlin, 459 pp..

Dutta, D., Ramachandran, A., and Leighton Jr., D.T. (2006) Effect of channel geometry on solute dispersion in pressure-driven microfluidic systems. Microfluid Nanofluid 2, 275-290.

Ferket, H., Swennen, R., Ortuño, S. and Roure, F. (2003) Reconstruction of the fluid flow history during Laramide forelandfold and thrust belt development in eastern Mexico: cathodoluminescence and δ18O-δ13C isotope trends of calcite-cemented fractures. Journal of Geochemical Exploration 78-79, 163-167.

Fookes, P., Gourley, C. and Ohikere, C. (1988) Rock weathering in engineering time. Quarterly Journal of Engineering Geology and Hydrogeology 21, 33-57.

Gomez-Rivas, E., Corbella, M., Martín-Martín, J.D., Stafford, S.L., Teixell, A., Bons, P.D., Griera, A. and Cardellach, E. (2014) Reactivity of dolomitizing fluids and Mg source evaluation of fault-controlled dolomitization at the Benicàssim outcrop analogue (Maestrat basin, E Spain). Marine and Petroleum Geology 55, 26-42.

Gohmmem, M., Zhao, W., Dyer, S., Qiu, X., and Brady, D. (2015) Carbonate acidizing: Modeling, analysis, and characterization of wormhole formation and propagation. Journal of Petroleum Science and Engineering 131, 18-33.

Goudie, A. S. (1999) Experimental salt weathering of limestones in relation to rock properties. Earth Surface Processes and Landforms, 24(8), 715-724.

Goudie, A.S., and Viles, H.A. (1997) Salt weathering hazards. Wiley, Hoboken, USA, 256 pp.

Graham, C., Lee, M., Phoenix, V. and Young, M. (2015) Conserving Scotland's Built Heritage: A Petrographic Investigation on the Effects of Deicing Salts on Scottish Sandstones. Engineering Geology for Society and Territory, Vol 8: Preservation of Cultural Heritage, 487-490.

Hamilton, A., Hall, C. and Pel, L. (2008) Sodium sulfate heptahydrate: direct observation of crystallization in a porous material. Journal of Physics D: Applied Physics 41, 212002.

Hamilton, A. and Menzies, R.I. (2010) Raman spectra of mirabilite, $Na_2SO_4 \cdot 10H_2O$ and the rediscovered metastable heptahydrate, $Na_2SO_4 \cdot 7H_2O$. Journal of Raman Spectroscopy 41, 1014-1020.

Jonas, L., John, T., King, H.E., Geisler, T. and Putnis, A. (2014) The role of grain boundaries and transient porosity in rocks as fluid pathways for reaction front propagation. Earth and Planetary Science Letters 386, 64-74.

Kar, A., Chiang, T.-Y., Ortiz Rivera, I., Sen, A. and Velegol, D. (2015) Enhanced Transport into and out of Dead-End Pores. ACS Nano 9, 8.

Kar, A., McEldrew, M., Stout, R.F., Mays, B.E., Khair, A., Velegol, D. and Gorski, C.A. (2016) Self-Generated Electrokinetic Fluid Flows during Pseudomorphic Mineral Replacement Reactions. Langmuir 32, 5233-5240.

Kelka, U., Koehn, D. and Beaudoin, N. (2015) Zebra pattern in rocks as a function of grain growth affected by second-phase particles. Frontiers in Physics 3.

Kelka, U., Veveakis, M., Koehn, D. and Beaudoin, N. (2017) Zebra rocks: compaction waves create ore deposits. Scientific reports 7, 14260.

Koehn, D., Malthe-Sørenssen, A. and Passchier, C.W. (2006) The structure of reactive grain-boundaries under stress containing confined fluids. Chemical Geology 230, 207-219.

Kondratiuk, P., Tredak, H., Ladd, A.J.C. and Szymczak, P. (2015) Synchronization of dissolution and precipitation fronts during infiltration-driven replacement in porous rocks. Geophysical Research Letters 42, 2244-2252.

Kondratiuk, P., Tredak, H., Upadhyay, V., Ladd, A.J.C. and Szymczak, P. (2017) Instabilities and finger formation in replacement fronts driven by an oversaturated solution. Journal of Geophysical Research: Solid Earth 122, 5972-5991.

Lichtner, P.C., Steefel, C.I. and Oelkers, E.H. (1996) Reactive transport in porous media. Mineralogical Society of America, Washington, DC.

Machel, H.G. and Buschkuehle, B.E. (2008) Diagenesis of the Devonian Southesk-Cairn Carbonate Complex, Alberta, Canada: Marine Cementation, Burial Dolomitization, Thermochemical Sulfate Reduction, Anhydritization, and Squeegee Fluid Flow. Journal of Sedimentary Research 78, 366-389.

Machel, H.G. and Mountjoy, E.W. (1986) Chemistry and Environments of Dolomitization - A Reappraisal. Earth-Science Reviews 23, 48.

Maliva, R.G., Budd, D.A., Clayton, E.A., Missimer, T.M. and Dickson, J.A.D. (2011) Insights into the Dolomitization Process and Porosity Modification in Sucrosic Dolostones, Avon Park Formation (Middle Eocene), East-Central Florida, USA. Journal of Sedimentary Research 81, 218-232.

Menon, G. and Otto, F. (2005) Dynamic Scaling in Miscible Viscous Fingering. Communications in Mathematical Physics 257, 303-317.

Merino, E. (2006) Self-accelerating dolomite-for-calcite replacement and displacive zebra veins: Dynamics of burial dolomitization. Geochimica Et Cosmochimica Acta 70, A417-A417.

Merino, E. and Canals, A. (2011) Self-Accelerating Dolomite-for-Calcite Replacement: Self-Organized Dynamics of Burial Dolomitization and Associated Mineralization. American Journal of Science 311, 573-607.

Montaron, B. (2008) Confronting carbonates. Oil Review Middle East 5, 132-135.

Nielsen, P., Swennen, R., Muchez, P. and Keppens, E. (1998) Origin of Dinantian zebra dolomites south of the Brabant-Wales Massif, Belgium. 1998 45, 17.

Ortoleva, P. (1994) Geochemical Self-Organization.

Ortoleva, P., Chadam, J., Merino, E. and Sen, A. (1987) Geochemical self-organization II: the reactive-infiltration instability. American Journal of Science 287, 32.

Pedrosa, E.T., Putnis, C.V. and Putnis, A. (2016a) The pseudomorphic replacement of marble by apatite: The role of fluid composition. Chemical Geology 425, 1-11.

Pedrosa, E.T., Putnis, C.V., Renard, F., Burgos-Cara, A., Laurich, B. and Putnis, A. (2016b) Porosity generated during the fluid-mediated replacement of calcite by fluorite. CrystEngComm 18, 6867-6874.

Petrus, K. and Szymczak, P. (2016) Influence of Layering on the Formation and Growth of Solution Pipes. Frontiers in Physics 3.

Plumper, O., Botan, A., Los, C., Liu, Y., Malthe-Sorenssen, A. and Jamtveit, B. (2017) Fluid-driven metamorphism of the continental crust governed by nanoscale fluid flow. Nat Geosci 10, 685-690.

Putnis, A. (1992) Introduction to mineral sciences. Cambridge University Press, Cambridge England ; New York.

Putnis, A. (2015) Transient Porosity Resulting from Fluid–Mineral Interaction and its Consequences. Reviews in Mineralogy and Geochemistry 80, 1-23.

Putnis, A. and Putnis, C.V. (2007) The mechanism of reequilibration of solids in the presence of a fluid phase. Journal of Solid State Chemistry 180, 1783-1786.

Putnis, C.V. and Mezger, K. (2004) A mechanism of mineral replacement: isotope tracing in the model system KCl-KBr-H2O. Geochimica et Cosmochimica Acta 68, 2839-2848.

Raufaste, C., Jamtveit, B., John, T., Meakin, P. and Dysthe, D.K. (2010) The mechanism of porosity formation during solvent-mediated phase transformations. proceedings of the Royal Society 467, 18.

Renard, F., Gratier, J.P., Ortoleva, P., Brosse, E. and Bazin, B. (1998) Self-organization during reactive fluid flow in a porous medium. Geophysical Research Letters 25, 385-388.

Robion, P., Humbert, F., Colombier, J.-C., Leghay, S. and de Lamotte, D.F. (2012) Relationships between pore space anisotropy and anisotropy of physical properties of silicoclastic rocks from the Corbières–Minervois fold-and-thrust-belt (north-east Pyrenees, France). Tectonophysics 576, 63-77.

Ruiz-Agudo, E., Putnis, C.V., Hövelmann, J., Álvarez-Lloret, P., Ibáñez-Velasco, A. and Putnis, A. (2015) Experimental study of the replacement of calcite by calcium sulphates. Geochimica et Cosmochimica Acta 156, 75-93.

Sachau, T., Bons, P.D. and Gomez-Rivas, E. (2015) Transport efficiency and dynamics of hydraulic fracture networks. Frontiers in Physics 3.

Sheng, J. (2010) Modern chemical enhanced oil recovery: theory and practice. Gulf Professional Publishing.

Spruzeniece, L., Piazolo, S. and Maynard-Casely, H.E. (2017) Deformation-resembling microstructure created by fluid-mediated dissolution-precipitation reactions. Nat Commun 8, 14032.

Steefel, C., Depaolo, D. and Lichtner, P. (2005) Reactive transport modeling: An essential tool and a new research approach for the Earth sciences. Earth and Planetary Science Letters 240, 539-558.

Steefel, C.I., Emmanuel, S., Anovitz, L.M., Mineralogical Society of America. and Geochemical Society. (2015) Pore-scale geochemical processes. Mineralogical Society of America ;, Chantilly, Virginia.

Szymczak, P. and Ladd, A.J.C. (2006) A network model of channel competition in fracture dissolution. Geophysical Research Letters 33, L05401.

Szymczak, P. and Ladd, A.J.C. (2009) Wormhole formation in dissolving fractures. Journal of Geophysical Research 114.

Szymczak, P. and Ladd, A.J.C. (2013) Reactive-infiltration instabilities in rocks. Part 2. Dissolution of a porous matrix. Journal of Fluid Mechanics 738, 591-630.

Whitaker, F.F., Smart, P.L. and Jones, G.D. (2004) Dolomitization: from conceptual to numerical models. Geological Society, London, Special Publications 235, 99-139.

Figures and caption

Figure 1 – KBr single crystal cut and used for the replacement, before first bath (a) and after 10 minutes of reaction and 2 X-CT scans (b). The blue colour of the preserved part of the sample comes from colour centres being activated by X-rays during the CT scans. The opaque white outer rim is the replaced K(Br,Cl) sample.

Figure 2 – Reconstructions of the X-CT dataset of a single crystal at the different reaction times: a) 3D-volume rendering of the crystal. The grey scale is is produced by absorption contrast where brighter areas are denser The scale bar represents 1 millimetre. b) 2D slice of a reaction front, extracted from dataset, location reported on (a). The black scale bar represents 200 micrometres. c) Results of data segmentation on a sub-volume parallel to (b). Light blue, red, deep blue and green pixels represent matter from the less dense to the densest, respectively. Porosity is represented in light blue; reaction zone is red and blue; unreacted KBr is green. Alongside we report the corresponding proportion of each domain as coloured number, along with the thickness of the domain 2 (see text and Fig. 3 for details). The dimension of the sub-volume is reported on the top image and is constant for all steps.

Figure 3 – 2D slice from a X-CT dataset of a single crystal of the set 2 experiment after 55 minutes of reaction time. a) The result of segmentation is represented in blue, illustrating the below-the-resolution issue. b) Zoom from the frame located in a), showing porosity which is impossible to segment because of the scan resolution. Arrows labelled length and width illustrate how the morphological measurements were carried out (results are reported in table 1).

Figure 4 – (a), (b) 2D view of volume rendering (left-hand side) along with interpretative representation (right-hand side) of the K(Br,Cl) replacement based on density absorption contrast after 10 minutes of reaction time (a) and after 35 minutes of reaction time (b). Assumed evolution of Cl substitution in the crystal is shown at the bottom of the figure.

Porosity is represented as transparent to light blue; replaced part is red; reaction front is darker blue; non-reacted KBr is green. These images are extracted from the volumes presented in figure 2c. (c) Observation under polarized light microscopy of a sample from a set I experiment cut following the scan performed after a reaction time t=15 min. The black frame in the upper image is the zoom window for the magnified image below.

Figure 5 – Results derived from X-CT scan segmentation and voxel counts, with interpretation of the trends. Corresponding error-bars from the standard deviation calculated on each dataset used to derive the average value, as described in the text. a) Plot of porosity (%) versus reaction time (minutes) considering the volume of pores in the reaction zone (circles), or the whole crystal (squares); with respect to the definition of the zones introduced in the text and Figs. 2 and 3. b) Plot of the relative initial KBr volume replaced by KBr,Cl (%) vs reaction time (minutes). Inset: Plot of the relative initial KBr volume replaced by KBr, Cl (%) vs square root of time ($minutes^{0.5}$). c) Plot of the relative mass loss (%) vs reaction time (minutes). Reported values are the measured mass after each scan. d) Plot of reaction zone thickness evolution (micrometres) vs the reaction time (minutes), with a separation between domain 2 (full circle) and domain 3 (empty circles). On the 4 graphs, coloured backgrounds correspond to an inferred realm of dominant reactive transport mechanism, and vertical dashed lines correspond to the change in transport regime. .

Figure 6 – Box and whisker plots of results derived from X-CT scans of set 2's batch 1 experiment, where only the pore were separated, labelled and their volume has been quantified (mm^3). A box and whisker plot comprises of 5 horizontal lines, corresponding

from bottom to top to: minimum value among the population, first quartile, median value, third quartile, and maximum value among the population. This representation of the pore volume distribution shows the detection limit, as well as the fact that the biggest pore volume increases with time during the replacement.

Figure 7 – 3D-views of pores (in blue) developing during experiment set 1. The volume of interest is reported as a frame.

Figure 8 – 2D-views of the same slice parallel to the KBr crystal top during set 1 experiment (a-e). Grey scale is related to absorption contrast (brighter is denser). f – density of fingers vs reaction time, measured parallel to the top of the crystal (squares) or perpendicular to the top of the crystal (circles).

Figure 9 - 2D-views and volume rendering of set 2 experiment: a KBr crystal after continuous reaction with saturated KCl solution after 15 minutes (a, b) and after 55 minutes (c, d) . Grey scale is related to absorption contrast (brighter is denser). Figure 9 clearly shows the formation of fingers perpendicular to the crystal wall.

Figure 10 – 2D-views of a crystal after complete replacement (5h30 minutes bath) showing the fingering process and the pore distribution in the central and outer regions of the crystal from top to bottom (contact between glass and crystal at the bottom,a) and on a slice view from top (c, location given on a). Grey scale is related to absorption contrast (brighter is denser). b) 3D volume rendering, with separation of the crystal (dark blue), empty pores (light blue) and clogged pores (red), location given on a.

Figure 11 – Results of a chemical model that calculates porosity increase during the KCl substitution in the solid KBr crystal (degree of replacement). Non-linear relationship is plotted as a solid line, and degree of substitution is inferred for the discontinuous experiment from porosity measured in the reacted zone, reported as circles and in the replaced zone, as crosses. This prediction method is validated by the comparison of the 35% porosity measured after 55 minutes of reaction in the replaced zone and the 50% of substitution in the same crystal observed by XRD.

Figure 12 – Conceptual sketch illustrating the effect of fingers (a) on the chemical gradient vs no fingers (b). The chemical gradient is represented as isocurves varying arbitrarily from a starting value of 1 (100% strongest chemical gradient at the fluid solid interface) to a value of 0 (lowest gradient- end of the reaction) with each consecutive curve separated by 0.2.

Figure 13 – Interpretative sketch summarizing the phenomenon driving porosity evolution in the case of the continuous experiment set (a-d1) and discontinuous set (a-d2). The bottom of the image is the KBr crystal face in contact with saturated KCl solution: a) represents the initial porosity created by the dissolution -precipitation mechanism, common in both the set 1 and 2 experiments. b) shows the proposed self-organization phenomenon during convective flow, the difference is the development of a mineral skin in the discontinuous set (b2). c1) shows the complete elongation of fingers until they interact with fingers growing from the orthogonal crystal face, while c2) shows the switch to a diffusion-dominated regime related to thickening of the poorly permeable crust. d1) and d2) represent the final steps in both systems where fingers coarsen and connect laterally.

Figure 1

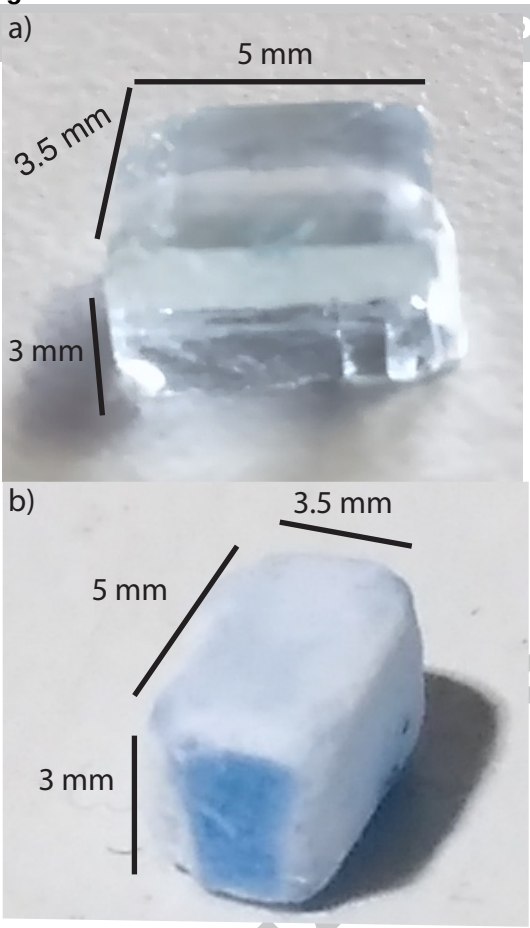

Figure 2

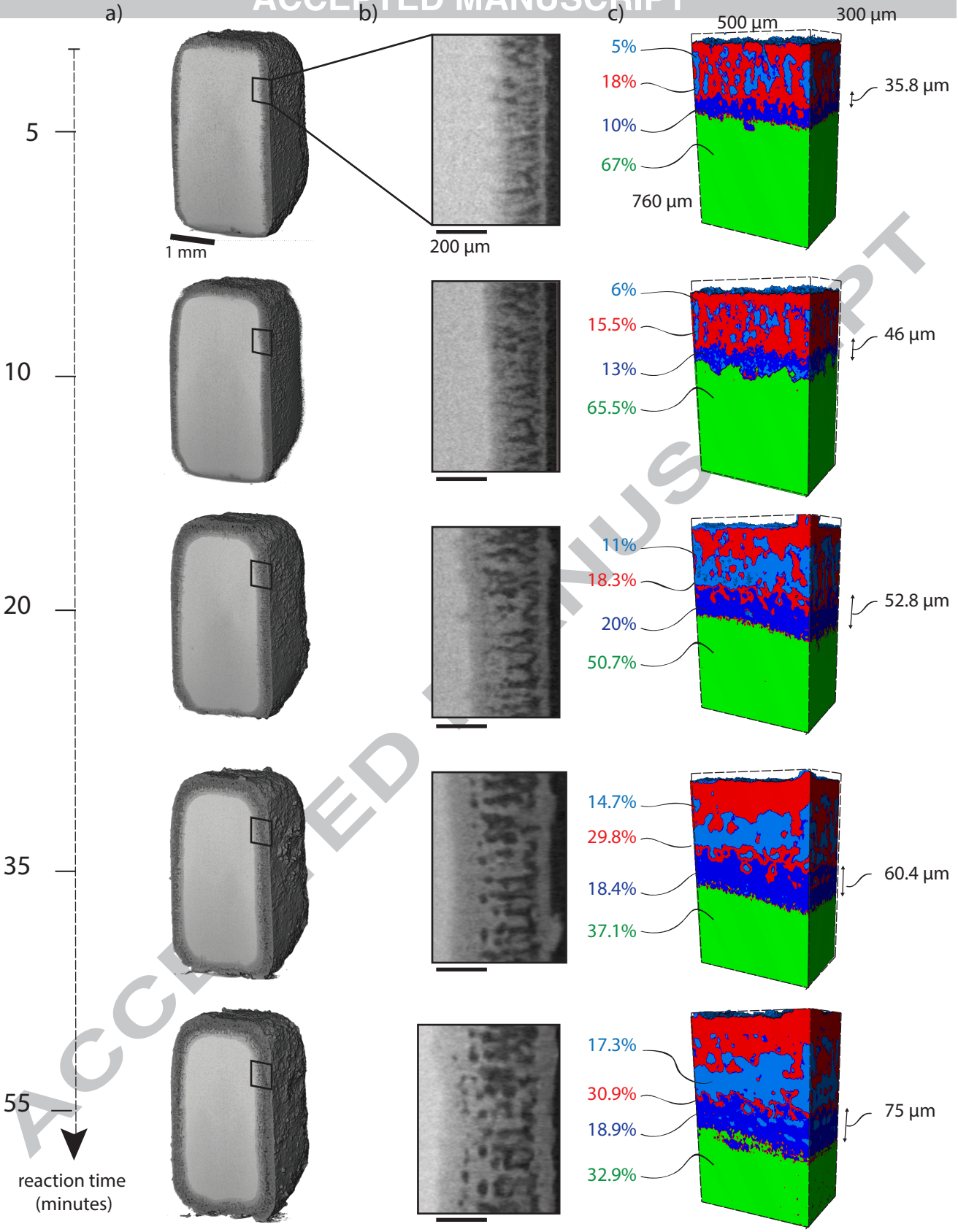

Figure 3

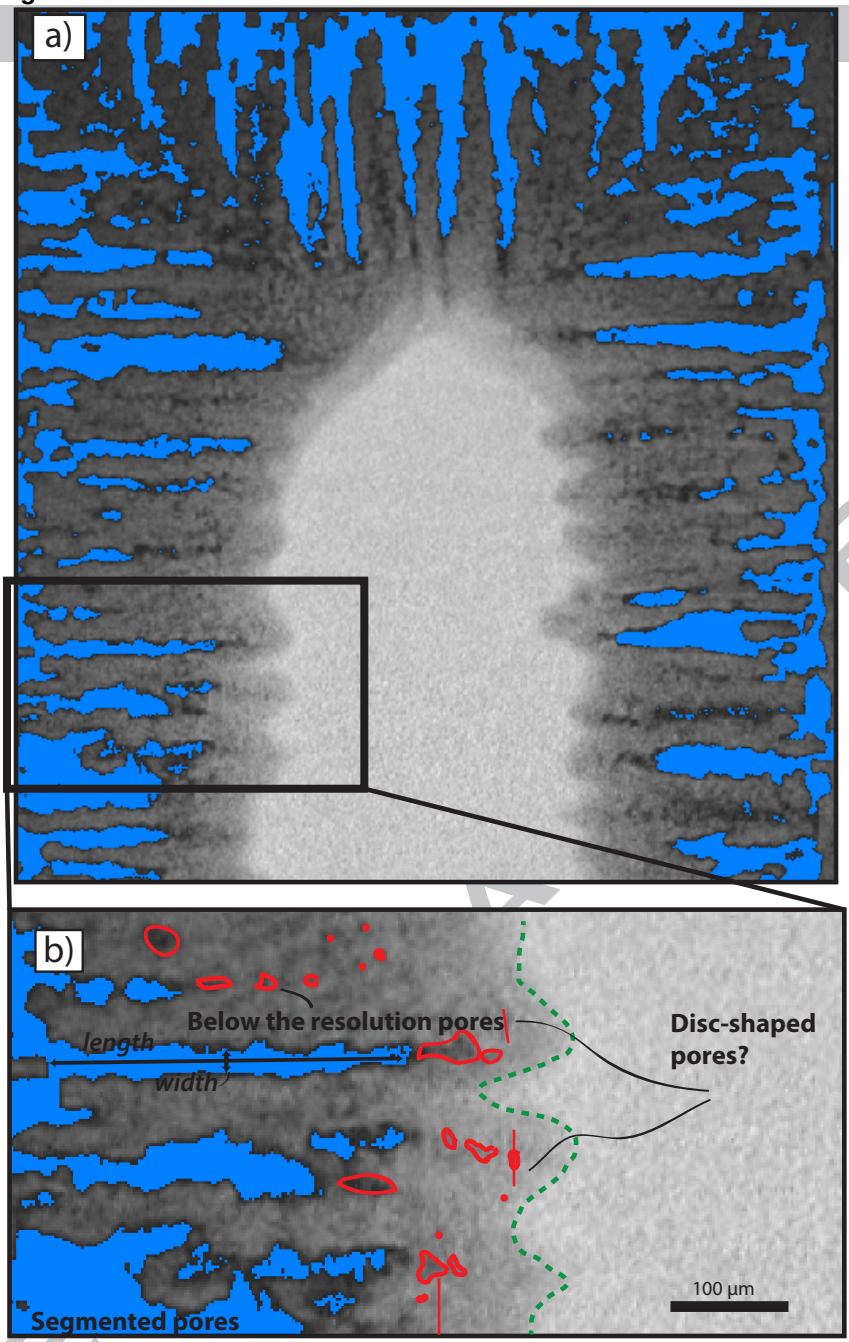
a)
b)
Below the resolution pores
length
width
Disc-shaped pores?
100 µm
Segmented pores

Figure 4

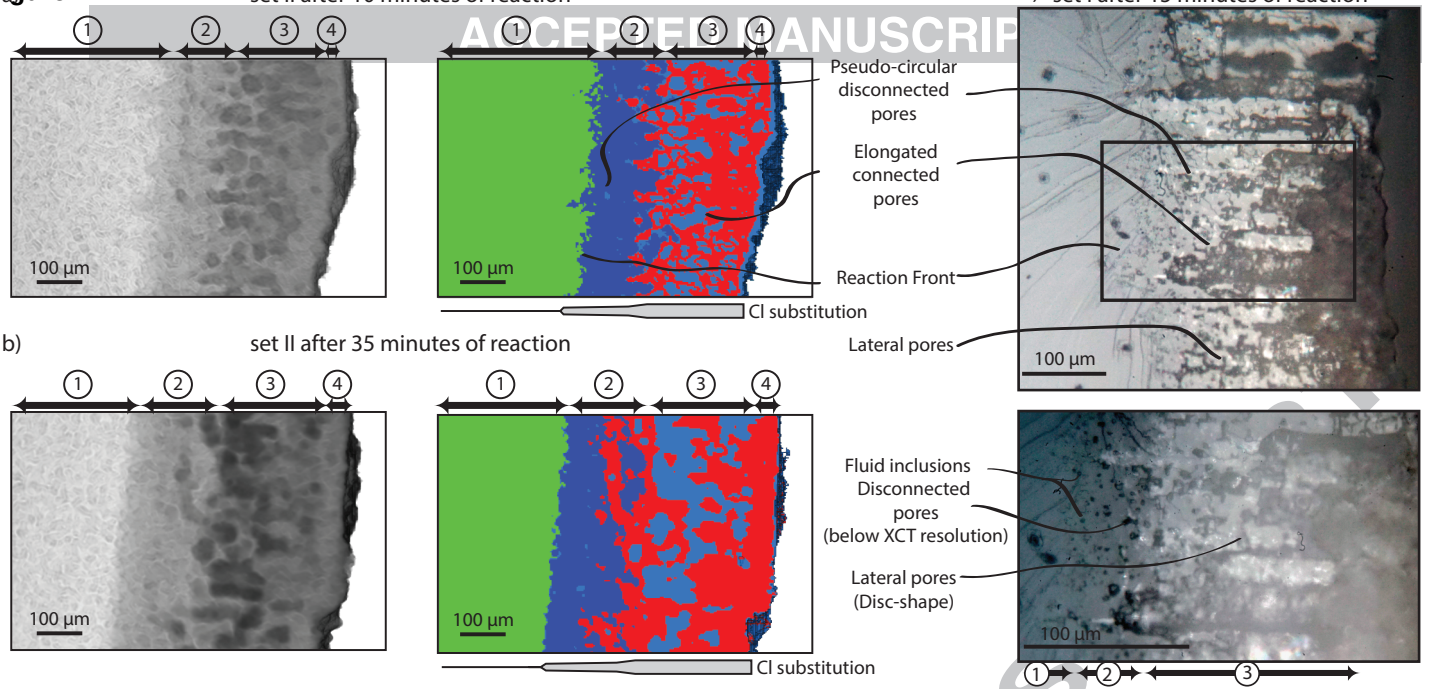

Figure 5

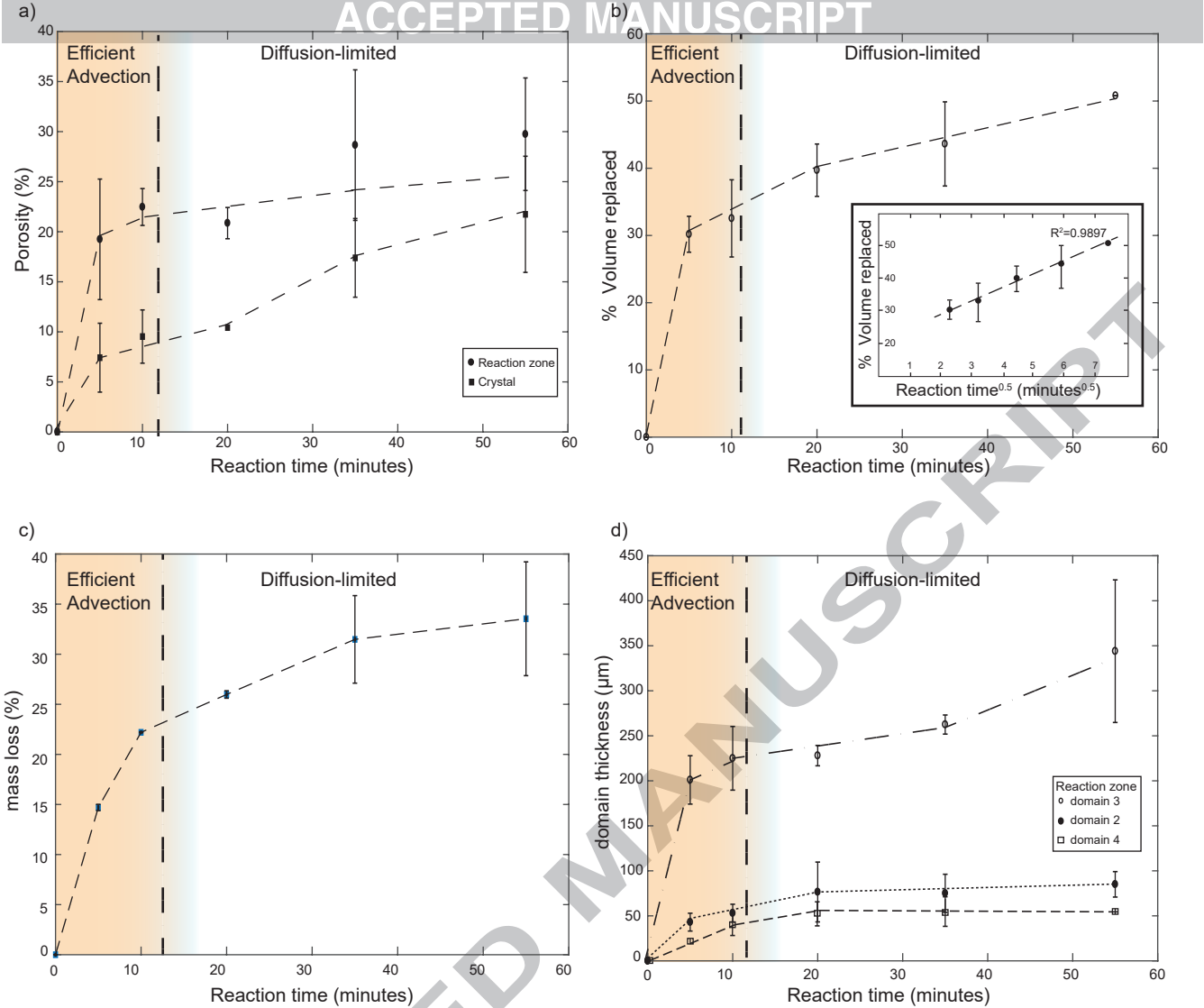

Figure 6

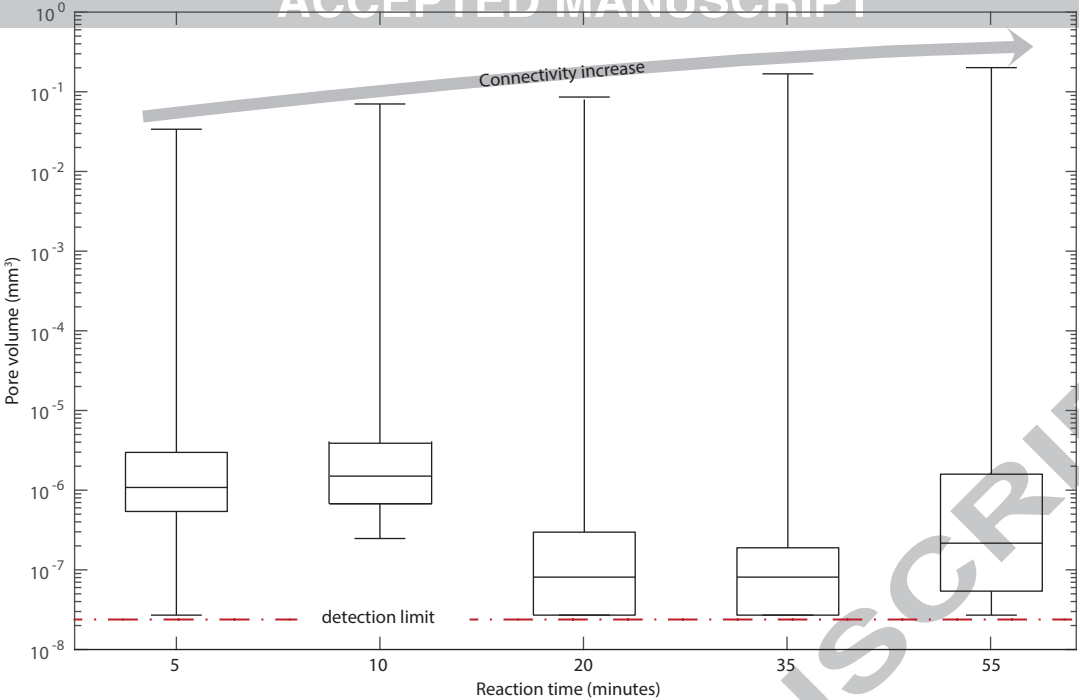

Figure 7

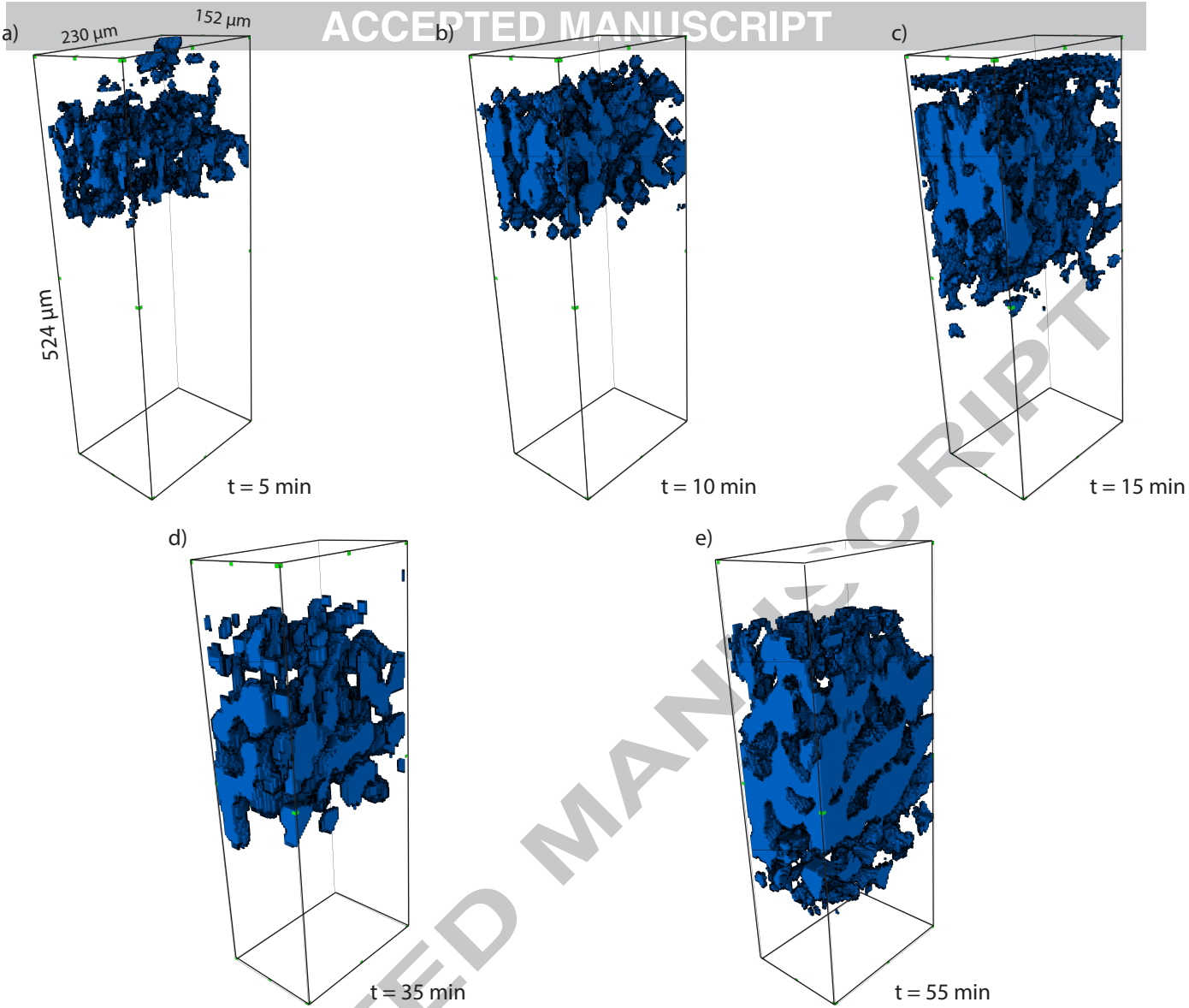

Figure 8

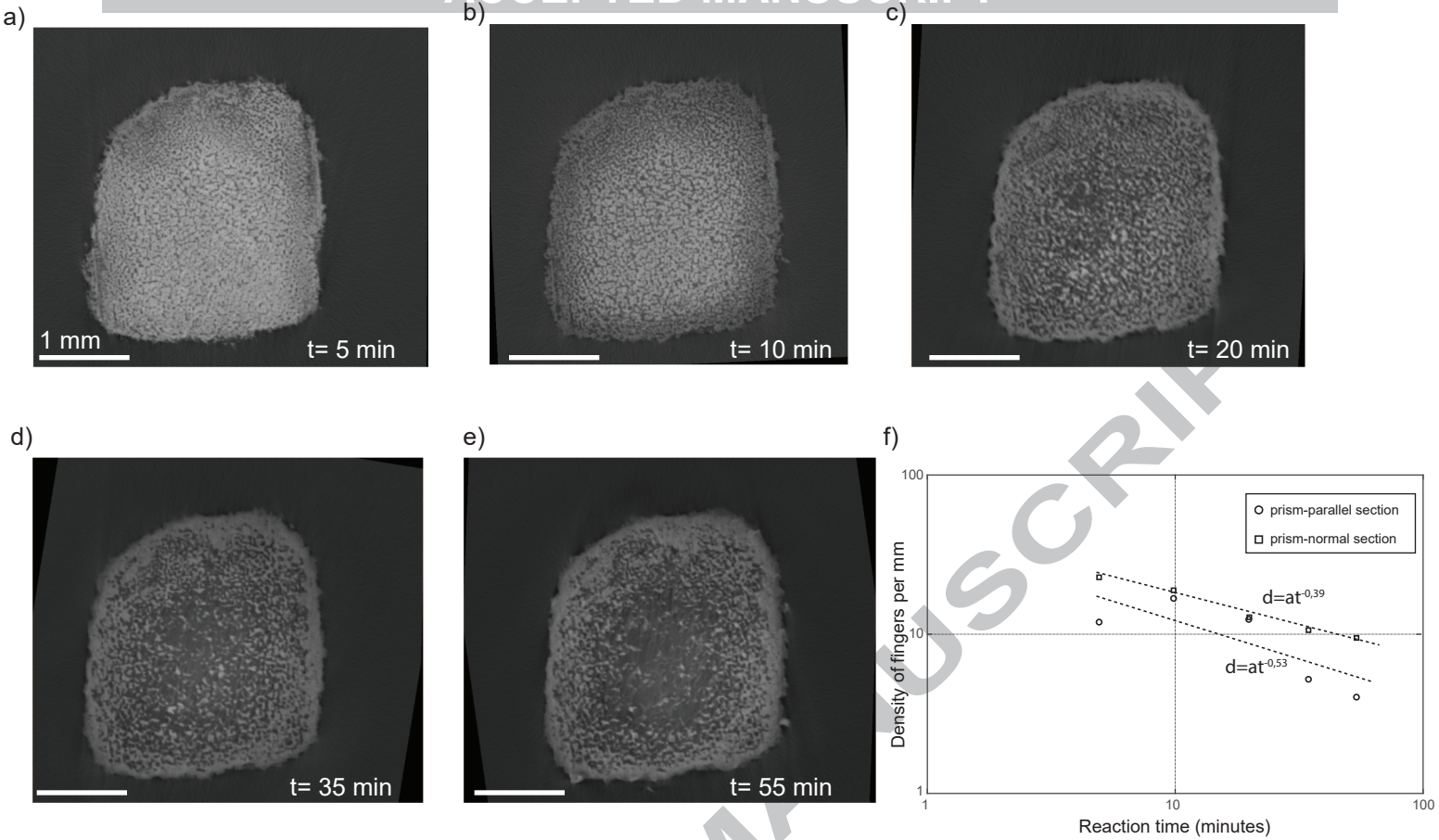

Figure 9

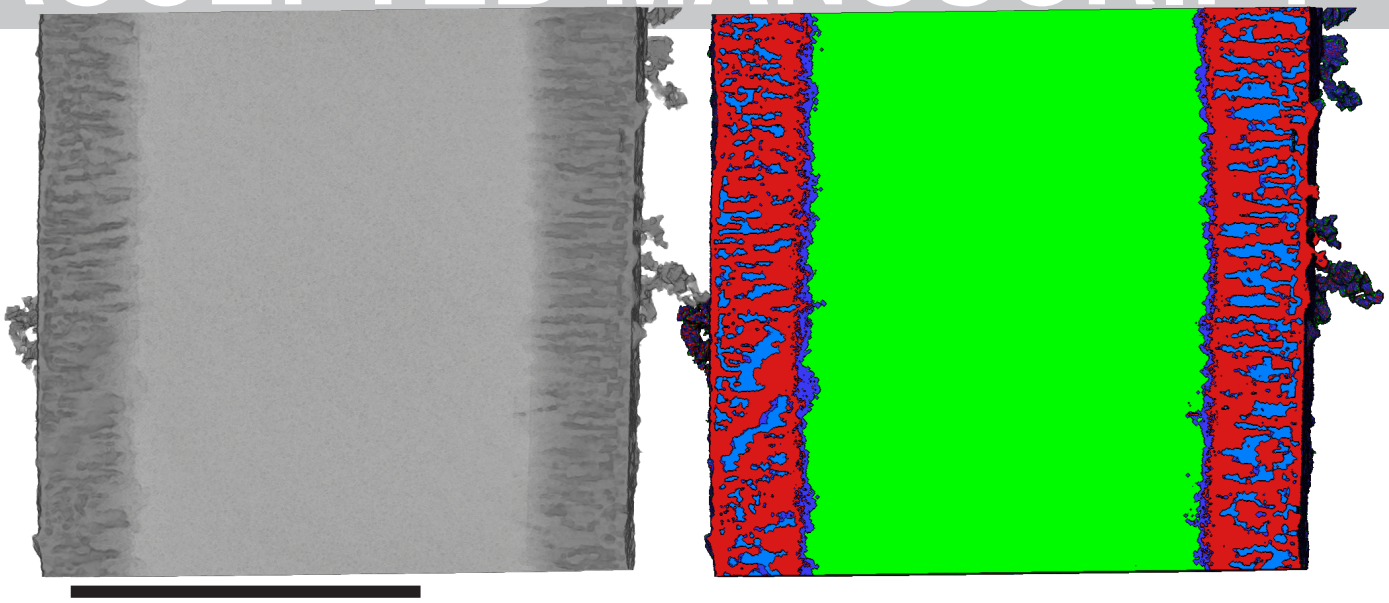

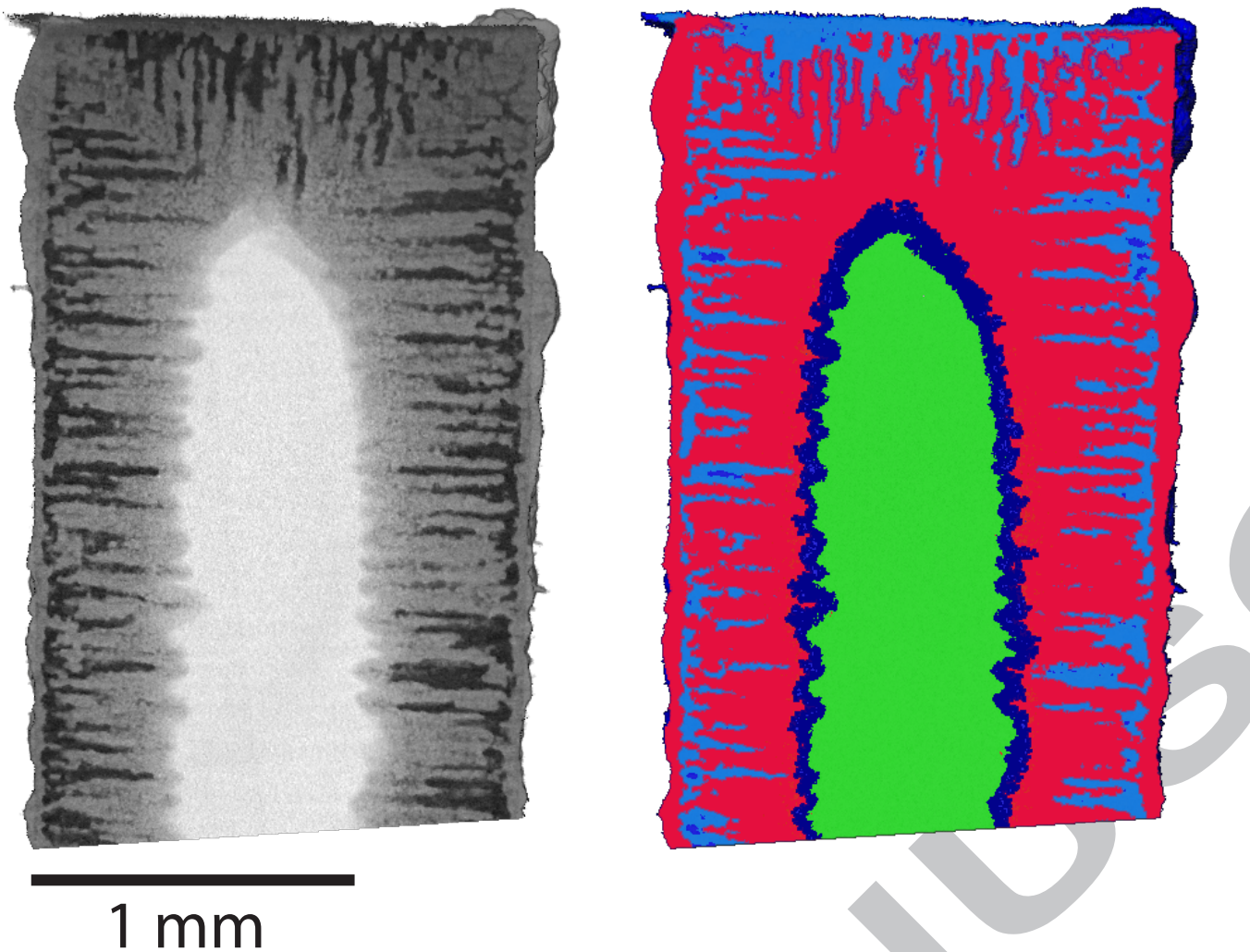

Figure 10

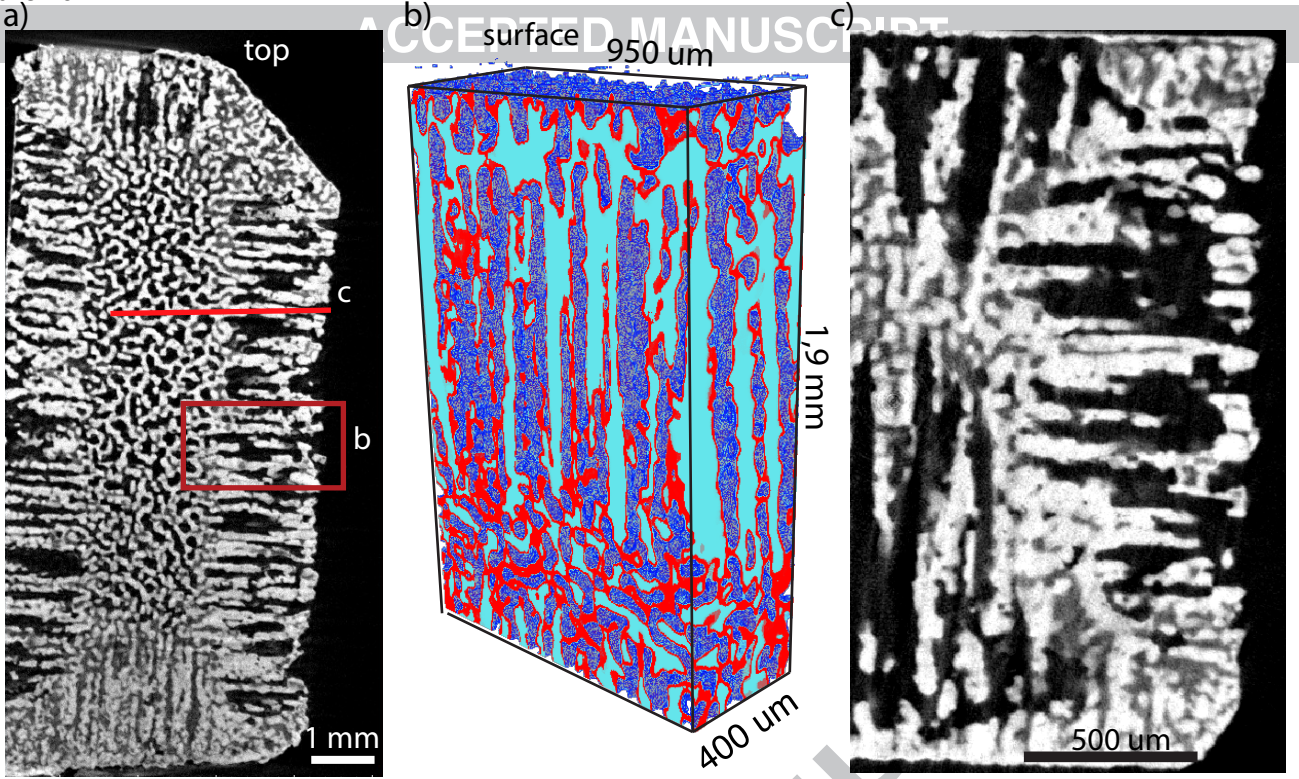

Figure 11

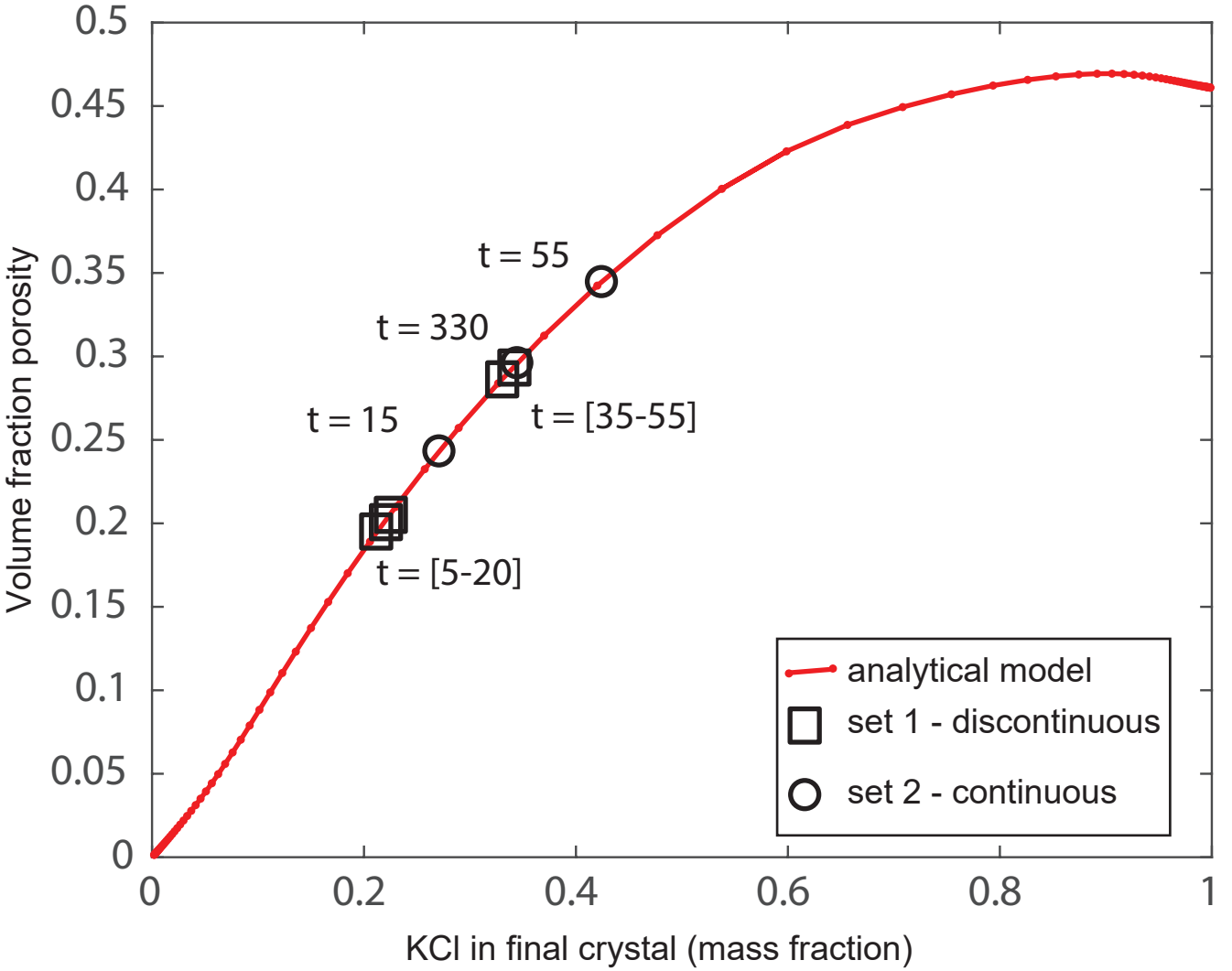
Volume fraction porosity
KCl in final crystal (mass fraction)
0.5
0.45
0.4
0.35
0.3
0.25
0.2
0.15
0.1
0.05
0
0
0.2
0.4
0.6
0.8
1
t = 55
t = 330
t = 15
t = [35-55]
t = [5-20]
analytical model
set 1 - discontinuous
set 2 - continuous

Figure 12

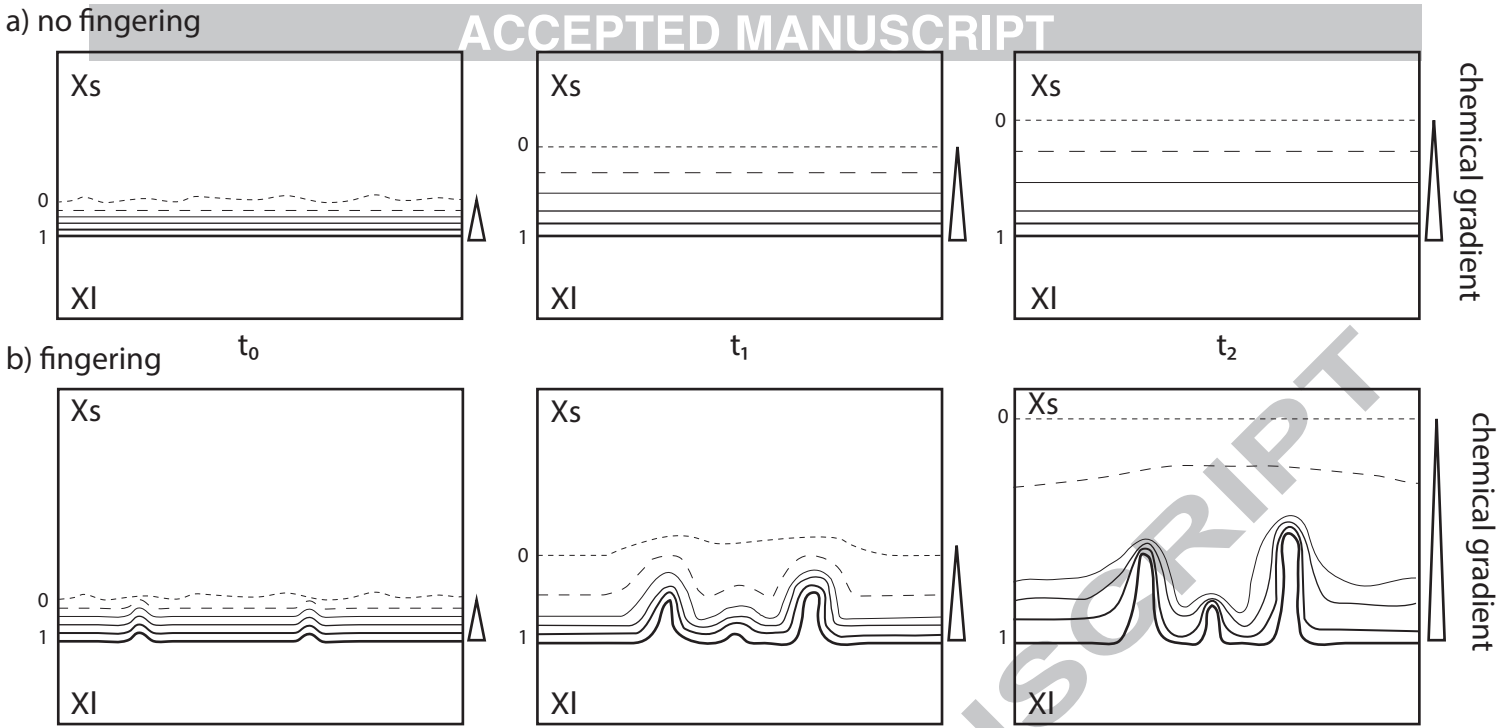

Figure 13

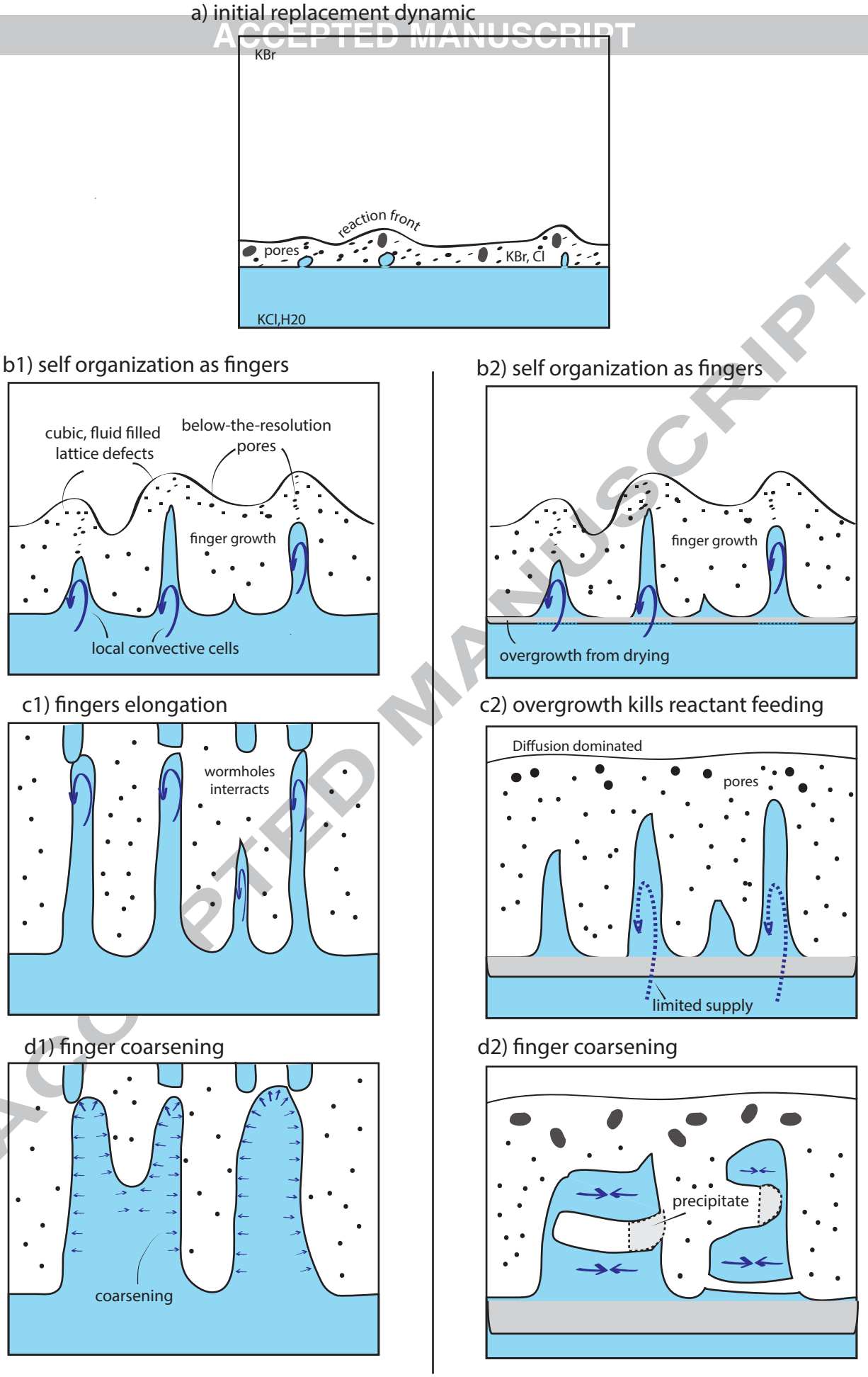

Table 1 – Mass of the crystal and volume of segmented phases after different reaction times for experiment sets 1 and 2.

Experiment Set	reaction time (min)	cumulative mass loss (mg)/corresponding percentage (%)		Reaction zone Domain 2				Reaction zone Domain 3				Volume of pores (mm^3)*		Porosi	
				Volume (mm^3)*		Thickness (µm)		Volume (mm^3)*		Average thickness (µm)					
		batch 1 (m0=97.2)	batch 2 (m0=110.5)	batch 1	batch 2	batch 1	batch 2	batch 1	batch 2	batch 1	batch 2	batch 1	batch 2	batch 1	ba
Set 1	0	0/0	0/0	0	0	0	0	0	0	0	0	0	0	0	
	5	14.5/14.9	16/14.5	2.565	1.624	36	50	4.649	6.553	182	220	1.271	2.512	14.98	
	10	21.6/22.2	24.5/22.2	3.996	3.205	46	60	3.267	6.128	200	250	1.95	2.911	21.17	2
	20	25/25.7	29/26.2	4.92	4.836	53	100	4.504	5.992	236	220	2.652	2.666	21.96	1
	35	27.6/28.4	38.2/34.6	4.676	2.301	60	90	7.575	7.693	255	270	3.727	5.142	23.33	3
	55	28.7/29.5	41.5/37.6	4.92	5.539	75	95	8.035	7.413	288	400	4.498	6.589	25.77	3
Set 2	15	19/24.4	17/25.2	2.06	1.63	70	35	4.89	9.2	350	420	3.62	2.42	30.8	1
	55	57.2/23.4	15.5/28.2	0.71	0.63	70	70	12.5	14.29	500	550	7.2	7.6	35.27	3
	330	30.5 /50	/	/	/	/	/	/	/	/	/	7.395	/	29	

*: Volumes are reported from measurements done in various volumes. All values are normalized to a volume of 25.5 mm3, Reaction zone volumes exclude the pore volume inside it